Journal of Electron Spectroscopy and Related Phenomena 178–179 (2010) 128–153

Contents lists available at ScienceDirect

Journal of Electron Spectroscopy and Related Phenomena

journal homepage: www.elsevier.com/locate/elspec

Review

Energy loss in XPS: Fundamental processes and applications for quantification, non-destructive depth profiling and 3D imaging

Sven Tougaard *

Department of Physics and Chemistry, University of Southern Denmark, DK-5230 Odense M, Denmark

ARTICLE INFO

Article history:
Available online 20 August 2009

Keywords:
XPS
Energy loss
Nano-scale quantification
Non-destructive depth profiling
3D imaging

ABSTRACT

Models for energy loss in XPS are reviewed. We start with rigorous models to describe the fundamental interaction of the electric fields from both the core-hole and the moving electron with the many-electron system of the solid and including also the influence of the surface and the interaction that takes place while the photoelectron moves in the vacuum. We then discuss the development of progressively simpler descriptions where different aspects of the rigorous model are treated approximately or ignored. These descriptions are less accurate but much more useful for practical data analysis. Applications for nano-scale quantification, non-destructive depth profiling and 3D imaging are discussed. The accuracy of the theory is in all parts validated by comparison to experiments.

Contents

* Tel.: +45 6550 3530; fax: +45 6615 8760.
E-mail address: svt@ifk.sdu.dk.

0368-2048/$ – see front matter © 2009 Elsevier B.V. All rights reserved.
doi:10.1016/j.elspec.2009.08.005

1. Introduction

X-ray photoelectron spectroscopy (XPS) is probably the most used method for quantitative characterization of elements at surfaces on the nano-meter depth scale [1,2]. The reason is that the typical distance λ between inelastic-scattering events for electrons of energies between 100 and 2000 eV (which are typical for XPS) is of the order of 1 nm [3–6]. If elastic scattering is neglected, measured emitted electron intensities $I(z)$ are then attenuated exponentially as a function of distance $z/(\lambda\cos\theta)$ to the surface according to

$$I(z) = I_0 e^{(-z/\lambda\cos\theta)} \quad (1)$$

where θ is the angle of emission with respect to the surface normal. With $\lambda \sim 0.5$–2 nm, XPS is thus ideal for the study of the outermost few nm.

It turns out that the presence of the surface may cause considerable changes in the energy loss spectrum as well as in the peak intensity [7–9]. The change in peak intensity can conveniently be described by a simple parameterization where the surface excitation is expressed as the extra probability for an energy loss event when the photoelectron crosses the surface. This effect is not huge but has received considerable interest in the past few years [10–16].

For quantitative XPS it has been, and still is, quite common to assume that the peak intensity is representative for the amount of atoms that are on or in the near-surface region. This is however far from being the case. The fundamental flaw is clear from Fig. 1 [17]. In the right-hand panel, model spectra of Au4d have been calculated for different depth distributions of a 1 nm thick gold layer. The same amount of Au atoms gives a hugely varying intensity because electrons excited at larger depths have a smaller probability (by Eq. (1)) of surviving at the peak energy but are likely to lose energy and end up at lower energies in the spectrum. This is clearly seen as an increase in the intensity below the peak energy and a corresponding decrease in the Au4d peak intensity as the 1 nm thick gold layer is buried at increasingly larger depths. The left-hand panel shows model spectra of Cu2p corresponding to four different surface morphologies of Cu atoms in an Au matrix. The XPS peak intensity from all four solids is identical although the surface compositions are very different. Analysis of these spectra under the assumption that the surface concentration is proportional to the peak intensity, would result in an inaccurate quantification as the true concentration at the surface could be anywhere from 0% (as in (c) and (d)) to 100% (as in (a)) and the true total amount of copper material within the surface region could be anywhere from the equivalent of 1.1 Å (as in (a)) or 10 Å (as in (c)) or even higher (as in (d)). These two examples show that there is actually very little quantitative information in the peak intensity. If the nano-structure of the sample is known in advance it is a simple matter to take these effects into account using Eq. (1) and obtain an accurate analysis. However this is of course not possible because the nano-structure is hardly never known in advance because it is exactly the purpose of the XPS analysis to determine that. From Fig. 1, it is however clear that both the peak intensity and the peak-shape vary strongly and it is very easy experimentally to distinguish between the spectra in a 50 eV energy region below each peak. This effect has been used to greatly improve XPS quantification [17–23].

It is thus clear that it is very important to understand electron energy-loss processes in XPS spectra. There are two origins to the energy-loss structure. The first is due to the sudden creation of an electric field from the core-hole created after photoexcitation of the electron. This field excites valence electrons and the excitation energy is lost by the photoelectron. Secondly the electric field from the photoelectron will, as it moves towards the surface, also cause excitations and thereby energy loss and such processes occur even after the photoelectron has left the surface. The corresponding energy loss processes are usually called “intrinsic” and “extrinsic” excitations, respectively [24–28].

Model calculations of energy loss in XPS have been done from first-principles quantum-mechanical descriptions [29–42] and these have been extremely valuable to enlighten the fundamental mechanisms behind the photoexcitation process. But the complexity of this approach makes it impractical for calculations other than for the free-electron-like solids. A more feasible semi-classical model [9] has been used in recent years [42–45] in which the interaction of valence electrons with the field from both the static core-hole and the moving photoelectron is described by the dielectric function of the medium. With this model, extensions beyond the nearly free-electron-like materials are straightforward because the only input in the calculations is the dielectric function. A major step forward in the practical application of this model has been the parallel development of methods to deduce the dielectric function from experimental Reflection Electron Energy Loss Spectra (REELS) for solids of any composition and even from nano-meter thin films [8,46–48]. This dielectric-response XPS model has been shown to describe experimental XPS quantitatively quite well [9,42–45]. User-friendly software has been developed [49] which facilitates the calculations and this is useful for investigations of the fundamental excitation mechanisms in XPS. But this is still a fairly complex analysis procedure which is not useful for practical, routine XPS analysis.

The description of XPS becomes much simpler if one assumes a complete decoupling of intrinsic, extrinsic, surface effects and excitations when the electron moves in the vacuum. In this model, the photoemission process is considered to be separable into two or three processes, i.e. first the core-electron is excited followed by the second step in which the electron is transported to nearby the surface and finally, in the third step, it escapes through the surface region and travels in the vacuum to the electron energy analyzer. A further simplification is obtained in the two-step model, where the excitations in the third step are replaced by the bulk excitation cross-section for paths up to the surface–vacuum interface and the excitations while the electron travels in the vacuum are ignored. Although the extrinsic/intrinsic contributions to the energy-loss structure vary considerably with energy, geometry and depth, it turns out that the two-step model is valid to describe the *changes* in both peak intensity and energy loss structure caused by variations in the depth distribution of excited electrons.

To calculate the change in the energy spectra in the two-step model, it is necessary to know the inelastic-scattering cross-

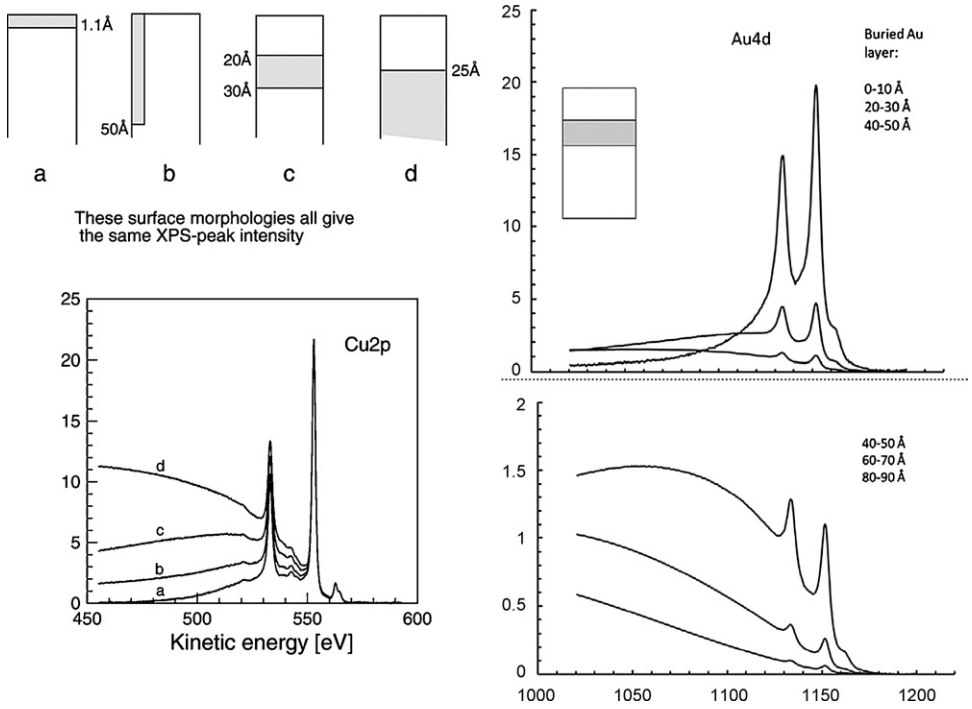

Fig. 1. Left panel: four widely different surface and near-surface distributions of Cu atoms in and on Au that give identical Cu XPS peak intensities, but quite different inelastic backgrounds, from [17]. Right panel: Au4d spectra from samples where the same 1 nm thick Au film is placed at increasingly larger depths in a Cu matrix.

section. This may be calculated from the dielectric function [7,50] of the solid or by analysis of a REELS spectrum [51,52]. However in practical samples, the composition varies along the path the electron follows which complicates the description considerably and the introduction of the concept of Universality classes of cross-sections [53,54] was an important step for practical modeling of the energy loss in XPS. Although these will not account for the finer details, they turn out to be sufficiently accurate to describe the main changes.

Rigorous algorithms to calculate the XPS energy spectra within the two-step model were developed a long time ago [17,18,20–23,55,56]. From this, quite detailed quantitative information can be determined from the XPS spectra. There are two different but equivalent approaches for quantitative nano-composition analysis within the two-step model. Either one starts with an intrinsic spectrum and calculates the changes due to extrinsic energy loss and compares the resulting spectrum on an absolute scale to the measured XPS (software to simulate this energy loss is available [57,58]). The extrinsic contributions will vary with the depth distribution of photoemitting atoms and by trial and error this depth distribution is determined. In the other approach, one corrects the measured XPS spectrum for the extrinsic contributions and determines the intrinsic XPS spectrum. This spectrum can be compared to a standard spectrum determined from analysis of a spectrum from a sample with known depth distribution. Usually (but not necessarily), a sample with homogeneous depth distribution is used. Again the depth distribution of atoms is varied until a good match between the two intrinsic spectra is obtained.

User-friendly software [58] has been developed which makes this technique available also for the non-specialist. Since XPS is generally non-destructive and all information is found from analysis of a single spectrum, it is possible to monitor composition changes on the nano-scale as they happen. Thus it is very easy to follow the evolution of nano-structures as, e.g. more material is sequentially deposited onto a surface or to study the gradual change in morphology as a consequence of, e.g. chemical reactions or annealing.

Application of this formalism is, in principle, straightforward. However since operator interaction is necessary, it is not well suited for automated data processing. Automation is particularly important for routine analysis and in XPS imaging where thousands of spectra must be analyzed. Such an algorithm was suggested recently [59,60]. It provides quantitative information on the atom depth distribution as well as on the number of atoms within the outermost ~10 nm. Its validity has been tested experimentally [60] and it was recently shown to successfully provide quantitative 3D XPS images [61–63]. Besides the application in 3D nano-imaging it is expected that this algorithm will be useful in the development of expert systems for automatic XPS analysis.

The above topics will be discussed in this paper.

2. Photoelectron spectra

In the simplest interpretation of XPS, a one-electron wave function is used in the “sudden approximation” and the effects of the surface are neglected. Although this approach is not strictly valid (see below), many of the practical applications of XPS for quantitative determination of composition and depth profiles can actually be quite well explained by this model (see below). However, for a fundamental understanding of the photoelectron intensity and energy spectrum, it is essential to consider a model that includes many-electron and surface effects. The energy-loss structure originates from both the static core-hole created during the photoexcitation of the core-electron and by the excitations that take place during transport of the photoelectron in and out of the solid. The corresponding energy-loss processes are usually called “intrinsic” and “extrinsic” excitations. Intrinsic (also called shake-up) excitations can sometimes be seen as distinct peaks on the low kinetic energy side of the main photoelectron peak. Several models have been proposed in the past for evaluation of XPS spectral line shapes [9,29–42]. Most models have been based on a quantum-mechanical description of the perturbation induced by the photoexcitation process of the electron states of the solid. A review on this subject was recently reported [39]. This first-

principles approach has been extremely valuable to enlighten the fundamental mechanisms behind the photoexcitation process. But the complexity of this approach makes it impractical for calculations of XPS for solids other than the free-electron jellium-type solids (see example in the upper panel of Fig. 4 below). It is, however, only for a few solids that electronic excitations can be quantitatively described within this model and, in general, it is insufficient. A method which makes calculations practically manageable for general materials, was proposed in [9]. In this semi-classical model, the interaction of the medium with the core-hole and the effect of the surface, as well as the excitations that take place during transport of the electron, are described by the complex dielectric function of the medium. A clear advantage of this dielectric-response description over the quantum-mechanical models, is that extensions beyond materials that can be described by the nearly free-electron model are straightforward because the only input in the calculations is the dielectric function. This is of paramount importance for practical applications because, as mentioned above, very few materials are well described within the free-electron model.

2.1. Dielectric-response model of XPS

The basic mechanism in the dielectric-response description is that the static core-hole as well as the moving photoelectron induces a potential in the medium. The photoelectron is in turn affected by this potential and this leads to energy-loss processes in which energy $\hbar\omega$ and momentum $\hbar k$ are transferred to the valence- and core-electrons of the solid. The variation in time and space of the induced potential is conveniently described by the complex dielectric function $\varepsilon(k,\omega)$ of the medium. For an electron traveling in an infinite medium we define by $K(E_0,T)$ the differential inelastic electron scattering cross-section, i.e. $K(E_0,T)dRdT$ is the probability that an electron of energy E_0 will lose energy in the interval $T, T+dT$ after having traveled a path length dR in the solid. This is given by [7,50]

$$K(E_0,\hbar\omega) = \frac{1}{\pi a_0 E_0}\int \frac{dk}{k} Im\left\{\frac{1}{\epsilon(k,\hbar\omega)}\right\} \quad (2)$$

where $\hbar\omega = T$, E_0 is the initial energy of the electron, a_0 is the Bohr radius, and k is the wave vector transferred from the electron. $k_\pm = (2m/\hbar^2)^{1/2}[E_0^{1/2} \pm (E_0-\hbar\omega)^{1/2}]$ are the limits of integration over k, imposed by energy and momentum conservation in the inelastic-scattering process.

The complex dielectric function of the medium is conveniently described by an expansion in terms of oscillators [52,64]:

$$Im\left\{\frac{1}{\varepsilon(k,\hbar\omega)}\right\} = \theta(\hbar\omega - E_g)\sum_{i=1}^{n} \frac{A_i\gamma_i\hbar\omega}{\left(\left(\hbar\omega_{0i}+\alpha_i\frac{\hbar^2k^2}{2m}\right)^2-\hbar\omega^2\right)^2+(\gamma_i\hbar\omega)^2} \quad (3)$$

where A_i, γ_i and $\hbar\omega_{0i}$ are the strength, width and energy position of the ith oscillator. The dispersion for each oscillator is α_i. For a free-electron-like material such as Al, $\alpha_i = 1$, while $\alpha_i \sim 0$ for core-electrons and for wide-gap insulators like SiO_2 [65,66] because of the typical weak k-dispersion for the corresponding electron energy bands. The step function $\theta(\hbar\omega - E_g)$ is included to simulate the effect of a possible energy gap E_g because no energy-loss processes are possible for $\hbar\omega < E_g$. Eq. (2) describes the energy-loss processes of an electron moving in an infinite medium.

Fig. 2 shows schematic representations of different situations in which an electron interacts with the surrounding valence electrons in the medium near a surface [42,67]. Thus, Fig. 2a shows a static situation where the charge of an electron at rest is screened by the surrounding electrons of the solid and an electric field is set up. Fig. 2b shows the situation where the electron is moving in the solid and the screened charge lags behind the moving electron. This gives rise to a time-varying electric field and the electrons of the solid may interact with this field and be excited to states at higher energy. The excitation energy is taken from the moving electron which, in turn, loses energy. Fig. 2c shows the situation where the electron is approaching the surface. Here the spatial extension of the electric field is modified by the presence of the surface. After the electron has left the surface it will still induce charge redistributions in the solid and the electron will interact with this field and may thus still lose energy while it moves outside the solid in the vacuum as in Fig. 2d. Fig. 2e shows the situation where there is a static core-hole left behind at the point of excitation corresponding to a photon excited core-electron. The photoelectron will interact with the electric field from this static positive charge in the first few angstroms as it moves away which, in turn, will change the probability distribution for energy loss.

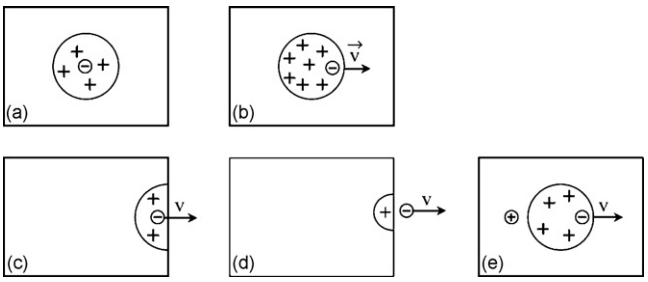

Fig. 2. Different experimental situations that give rise to different boundary conditions for the calculations of energy-loss processes, from [67].

2.1.1. Effects of the core-hole and of the surface

In the semi-classical model [9,42,67] based on a dielectric description of the electron energy losses of a photon excited core-electron, it is assumed that an electron-hole pair (both considered as point charges) is created at a given depth inside a semi-infinite medium, characterized by a dielectric function $\varepsilon(k,\omega)$. The calculation applies the "specular reflection model" [68,69] which allows one to solve the electrodynamic problem with the proper boundary conditions for the electric potential and field at the surface–vacuum interface. The geometry of the situation is defined in the inset in Fig. 3. The core-hole is assumed to be static with infinite lifetime, i.e. it remains at a fixed location forever after being created at time $t = 0$.

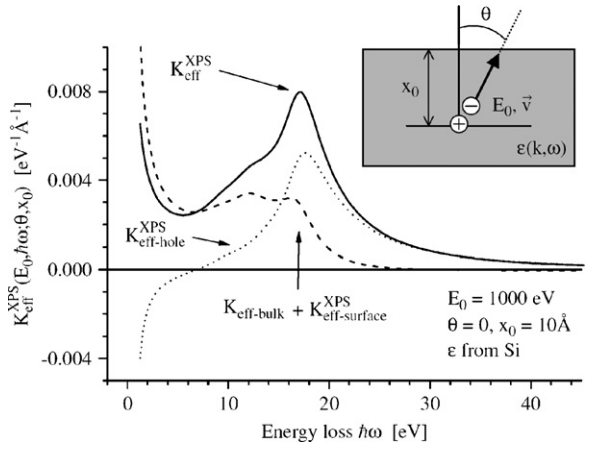

Fig. 3. Cross-section for emission in XPS (Si, $E_0 = 1000$ eV, normal emission, $x_0 = 10$ Å). The contribution to the losses induced by the static core-hole has been isolated from that of the moving photoelectron, from [67].

The photoelectron escapes from the semi-infinite medium with a velocity **v** in a rectilinear trajectory. Within this model, one defines an effective inelastic-scattering cross-section $K_{eff}(E_0,\hbar\omega;\varepsilon,\theta,x_0)$ in terms of the induced potential. $K_{eff}(E_0,\hbar\omega;\varepsilon,\theta,x_0)$ is defined as the average probability that a photoelectron excited at depth x_0 with energy E_0 shall lose energy $\hbar\omega$ per unit energy loss and per unit path length while traveling in the specified geometry. The energy loss includes processes that take place after the electron has left the surface but the average is taken over the path length traveled inside the solid, i.e. $x = x_0/\cos\theta$, where θ is the angle to the surface normal. Neglecting angular electron deflection one gets [9]

$$K_{eff}(E_0,\hbar\omega;\varepsilon,\theta,x_0) = \frac{2}{(2\pi)^4\hbar^2\omega x}\Re e\left\{\int dt\int d^3r\rho_e(\mathbf{r},t)i\int d^3k\,\mathbf{k}\cdot\mathbf{v}\Phi_{ind}(\mathbf{k},\omega;\varepsilon,\theta,x_0)e^{i(kr-\omega t)}\right\} \quad (4)$$

where **r** is the position, $\rho_e(\mathbf{r},t)$ the charge density of the escaping photoelectron, and $\Phi_{ind}(\mathbf{k},\omega;\varepsilon,\theta,x_0)$ the Fourier transform of the potential induced by the escaping photoelectron and the static core-hole in the semi-infinite medium.

The final expression for $\Phi_{ind}(\mathbf{k},\omega;\varepsilon,\theta,x_0)$, given in [9], has several terms which, from their dependence on the charge of the static hole, can formally be identified as being due to the static core-hole (denoted "hole" terms) and the rest which are independent of the hole (denoted "no-hole" terms) so that

$$\Phi_{ind}(\boldsymbol{k},\omega;\varepsilon,\theta,x_0) = \Phi_{ind,no-hole}(\boldsymbol{k},\omega;\varepsilon,\theta,x_0) + \Phi_{ind,hole}(\boldsymbol{k},\omega;\varepsilon,\theta,x_0) \quad (5)$$

This is a formal division and it is not strictly possible to make this distinction because the different contributions interfere. More details and the precise expressions for the "no-hole" and "hole" contribution to the total induced potential can be found in [9]. The expressions are quite involved and will not be repeated here. It is common to denote those excitations that are due to the potential $\Phi_{ind,hole}$ as "intrinsic" and those that are due to the potential $\Phi_{ind,no\text{-}hole}$ as "extrinsic". With this identification, the total cross-section is decomposed in the form:

$$K_{eff}(E_0,\hbar\omega;\varepsilon,\theta,x_0) = K_{eff}^{extr}(E_0,\hbar\omega;\varepsilon,\theta,x_0) + K_{eff}^{\mathrm{intr}}(E_0,\hbar\omega;\varepsilon,\theta,x_0) \quad (6)$$

where $K_{eff}^{\mathrm{intr}}(E_0,\hbar\omega;\varepsilon,\theta,x_0)$ is the sum of the terms that would disappear if the hole were not there and $K_{eff}^{extr}(E_0,\hbar\omega;\varepsilon,\theta,x_0)$ is the sum of the remaining terms. Note that with this separation into "intrinsic" and "extrinsic" excitations, these terms include the so-called "interference" effects that may be attributed to the interference between the fields from the core-hole and the moving electron. Since the interference effect diminishes the total energy loss, the intrinsic cross-section may be negative (see Fig. 3). The total cross-section is, however, always positive.

Fig. 3 shows an example of such a calculation [67] of the XPS from a photoexcitation of a Si core-electron to 1000 eV energy in a Si matrix at depth $x_0 = 10$ Å at normal emission. With the present notation, $K_{eff}^{extr} = K_{eff-bulk} + K_{eff-surf}^{XPS}$ and $K_{eff}^{\mathrm{intr}} = K_{eff-hole}^{XPS}$. Note that most of the bulk plasmon losses (seen as the peak at ~ 16 eV energy loss) are due to intrinsic excitations. Thus, less than half of the bulk plasmon intensity is caused by the extrinsic processes occurring as the electron is transported from 10 Å depth and out of the solid while the major part of the bulk plasmon intensity is intrinsic, i.e. caused by the static core-hole. Note that the only input in this calculation (which was done with the generally available software [49]) is the dielectric function for Si.

In an experimental XPS measurement, there will be contributions from photoelectrons excited at a range of depths. It is therefore necessary to account for their relative contributions to the spectrum. This is done by introducing an averaged effective cross-section [42]

$$K_{eff,av}(E_0,\hbar\omega;\varepsilon,\theta) = K_{eff,av}^{\mathrm{extrinsic}}(E_0,\hbar\omega;\varepsilon,\theta) + K_{eff,av}^{\mathrm{intrinsic}}(E_0,\hbar\omega;\varepsilon,\theta) \quad (7)$$

where the "extrinsic" and "intrinsic" contributions can each be estimated as a weighted average over the total pathlength x traveled by the electron inside the medium as

$$K_{eff,av}^{\mathrm{extrinsic/intrinsic}}(E_0,\hbar\omega;\varepsilon,\theta) = \int_0^\infty W(E_0;\varepsilon,\theta,a)K_{eff}^{\mathrm{extrinsic/intrinsic}}(E_0,\hbar\omega;\varepsilon,\theta,a)dx \quad (8)$$

The weight function $W(E_0;\varepsilon,\theta,a)$ takes into account the pathlength distribution of the electrons having suffered only a single inelastic-scattering event [42].

For comparison to photoemission experiments, the elastic peak must be included. If $F(E)$ is the primary excitation spectrum, the model spectrum $J(E)$ from a homogeneous sample corresponding to one inelastic-scattering event is given by

$$J(E) \propto F(E) + \lambda\int_E^\infty F(E')K_{eff,av}(E_0,E'-E)dE' \quad (9)$$

where $E' - E = \hbar\omega$. In order to be self-consistent with the calculated $K_{eff,av}$, λ is usually taken as the inverse of the area of $K_{eff,av}$ Thus, $J(E)$ represents the model XPS spectrum corresponding to a zero-loss peak $F(E)$ together with the single inelastic-scattering contribution. In practice, $F(E)$ can be taken as a mixed Gaussian–Lorentzian curve with a width given by the lifetime broadening of the excitation [42]. A software package is available that allows to do all these calculations [49].

In [38], the XPS dielectric-response model was compared to a quantum-mechanical calculation and Fig. 4 shows the comparison for Al and the dependence of the satellite spectra as a function

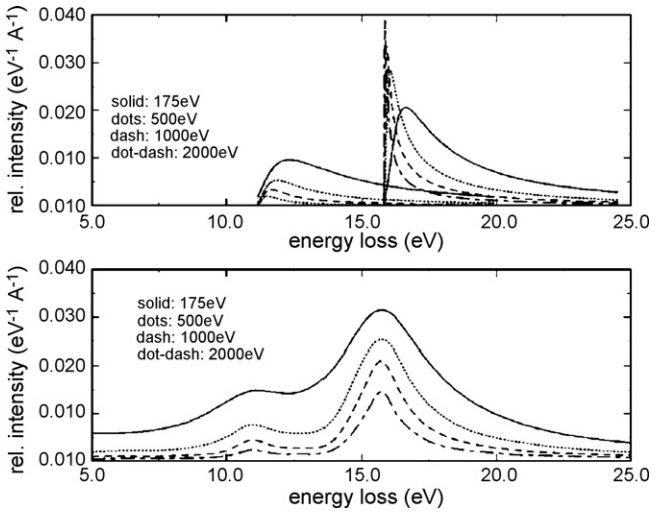

Fig. 4. Bulk and surface plasmon satellite spectra in Al according to a quantum-mechanical model (top curves) and the dielectric-response model (bottom curves) at various energies and normal emission, from [38].

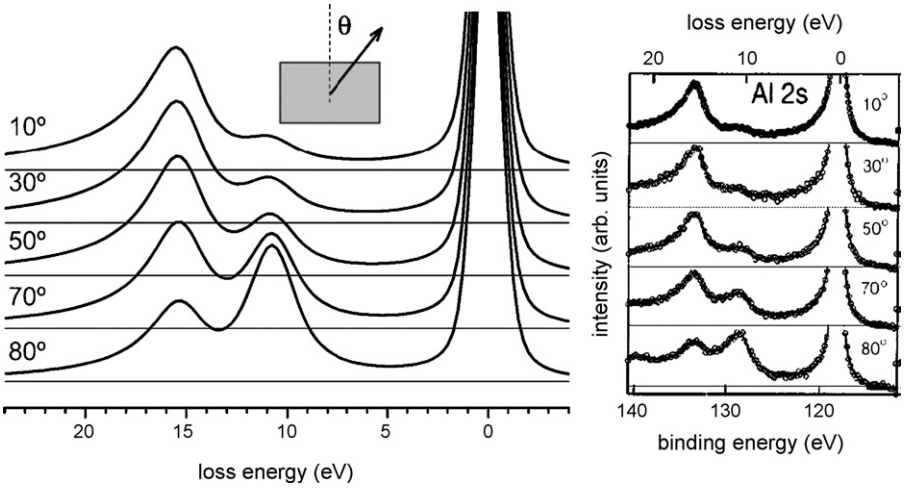

Fig. 5. Left: model photoemission spectra calculated according to Eq. (9) for photoelectrons traveling in Al with 1130 eV kinetic energy for several emission angles. Right: experimental results for A1 2s photoemission in Al sample from [70] for the same experimental conditions used in the model calculations, from [42].

of photon energy for normal emission. The surface contribution decreases relative to the bulk one, and the bulk peak becomes sharper with increasing energy. The trends roughly agree but the large broadening in the dielectric-response calculations, which is absent in the quantum-mechanical calculations, makes a quantitative comparison difficult [38].

2.1.2. *Experimental verification of the dielectric-response XPS model*

The validity of the dielectric model for the simulation of XPS spectral lineshapes has been investigated by comparison to experiments [9,42–44]. For example in [42] it was shown that the theory accounts well for the peak-shape observed in experiments [70] for angular dependence of the Al2s emission. The comparison is shown in Fig. 5 where the bulk and surface plasmons (at ∼15 and 10 eV, respectively) are clearly seen to depend strongly on the geometry, with the surface plasmon being more prominent for glancing emission angles.

The model calculations reproduces the absolute intensities as well as the shapes of both bulk and surface excitations for the whole series of experimental spectra taken at exit angles from 10° to 80°. The only fitting parameter in this model is the width of the elastic peak since the parameters that define the dielectric function were taken from independent experiments. The calculation scheme can easily be applied to other materials and experimental conditions. The only input in the calculations is the dielectric function which for a given solid may be taken from compilations [71] or it may be determined experimentally from a fairly simple analysis of REELS spectra using a dielectric-response model and accompanying software developed for this purpose [8,46,72].

In [42], the excitations were split into extrinsic and intrinsic contributions to the measured spectra. As was discussed above, these contributions are related to the electronic excitations due to the moving electron or to the core-hole, respectively. Fig. 6 shows that both extrinsic and intrinsic surface losses are enhanced with respect to the corresponding bulk losses at glancing emission angles. However, the change with angle of emission in the absolute contribution of extrinsic and intrinsic losses to $K_{eff,av}$ is different. For the "surface" losses (identified as the region around the peak at ∼10 eV), the "extrinsic" contribution to $K_{eff,av}$ accounts for more than 95% of the intensity for all studied angles of emission. Note that, as described above, the slightly negative intrinsic cross-sections in Fig. 6 are due to the "interference" effect [42].

For the bulk losses (identified as the peak at ∼15 eV and the accompanying tail) the relative intensity of "intrinsic" to "extrinsic" excitation varies with the emission angle. Thus ∼62% of the total area of the bulk plasmon is due to intrinsic losses at normal emission, while it is ∼35% at 80° [42]. The shape of the intrinsic losses is clearly different from the extrinsic. The intrinsic losses are more step-like in shape being very asymmetric with excitations that extend to much larger energy losses than the extrinsic losses (see Fig. 6). This shows that the characteristic asymmetric shape of the bulk plasmon peak which is observed in experiments is caused by the intrinsic contribution to the bulk plasmon while the extrinsic bulk plasmon has only a small asymmetry towards higher energy loss. The spectra taken at glancing angles have less intrinsic losses than those at normal emission. This is easily understood since, for

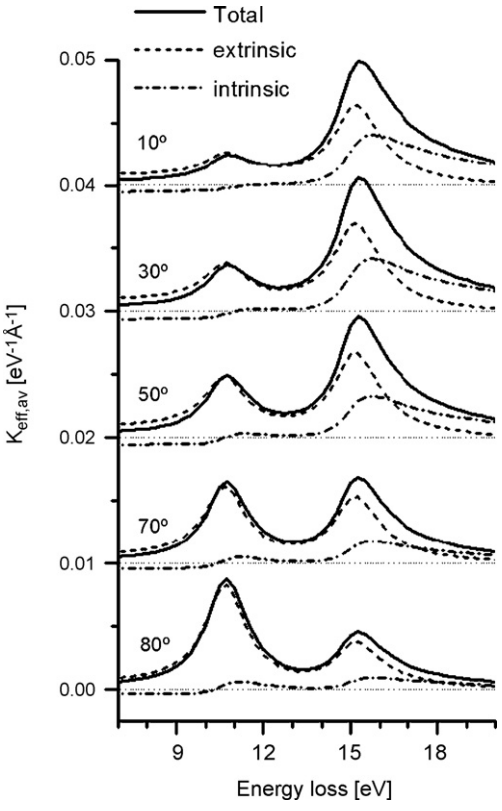

Fig. 6. Effective average cross-sections $K_{eff,av}$ corresponding to the model calculations in Fig. 5. The extrinsic and intrinsic contributions to the spectra are indicated as dashed and dot-dashed lines, respectively, from [42].

glancing angles the photoelectron loses more energy (to extrinsic excitations) while it moves in the vacuum above the surface where it interacts for a longer time with the electrons in the solid compared to an electron being emitted normal to the surface. Therefore the relative contribution of intrinsic excitations decreases with increasing emission angle. This is also likely to be the explanation why the surface excitations are almost purely extrinsic for all angles of emission because the extrinsic excitations that take place as the electron travels in the vacuum occur mostly at the surface plasmon energy [42].

Fig. 6 and Refs. [9,42,67] show that the extrinsic/intrinsic contributions to the energy loss structure vary considerably with energy, geometry and depth, and it is not strictly possible to separate the excitations due to the hole, the moving electron, and the effect of the surface. However, as it turns out, for energies >100 eV, this is in fact a useful and valid model to describe the *changes* in peak intensity and energy loss structure caused by variations in the depth distribution of excited electrons. It is these *changes* that are most important for practical quantitative XPS. This model will now be discussed.

3. The two- and three-step models of XPS

The description of XPS becomes much simpler if one assumes a complete decoupling of intrinsic, extrinsic, surface effects and excitations when the electron moves in the vacuum. In this model, the photoemission process is considered to be separable into two or three processes, i.e. first the core-electron is excited by the incoming photon at the atoms that are located at different depths z (Fig. 2e). This spectrum (denoted $F(E)$ in the following) includes the intrinsic excitations and its shape is determined by the lifetime of the core-hole and interactions of the static core-hole with the valence electrons as were discussed in Section 2. This is followed by the second step in which the electron is transported to nearby the surface (Fig. 2b). In this step, the energy spectrum is modified by inelastic-scattering events, i.e. extrinsic excitations which are evaluated according to the bulk cross-section (Eq. (2)). Finally, in the third step, it escapes through the surface region and travels in the vacuum to the electron energy analyzer (Figs. 2c and d). If one is not interested in the detailed XPS energy spectrum but only in the peak intensity, one can conveniently describe the excitations in the third step by the surface excitation parameter P_S (see Section 3.5.1).

3.1. Two-step XPS model

The excitations in the third step are complex, because as was discussed in Section 2, starting from depths slightly below the surface the probability for bulk excitations gradually decrease and the probability for surface excitations increase and then after the electron has left the surface, there is still a probability for energy loss due to interaction with the valence electrons in the surface region. These complications are avoided in the two-step model, where the excitations in the third step (i.e. as the electron travels in the surface region and the vacuum) are replaced by the bulk excitation cross-section for paths up to the surface–vacuum interface and the excitations in the vacuum are ignored.

Within this two-step model, if $F(E_0,\Omega)d^2\Omega dE_0$ denotes the flux of electrons excited from an atom in an energy interval dE_0 at E_0 into the solid angle element $d\Omega$, then the number of electrons emitted per second, per unit energy and solid angle Ω is given by [18]

$$J(E,\Omega) = \int dE_0 F(E_0,\Omega) \int f(z) G(E_0, \frac{z}{\cos\theta}; E) dz \tag{10}$$

where $G(E_0,R;E)dE$ is the probability that an electron with initial energy E_0 has energy in the interval E, $E+dE$ after having traveled the path length R, and $f(z)$ is the number of atoms per unit volume at depth z. In Section 3.3, algorithms to calculate G are considered.

For energy spectra where the total energy loss is small compared with the primary electron energy, $K(E,T) \cong K(T)$, independent of E. In this case, Landau [73] showed that

$$G(E_0, R; E) = \frac{1}{2\pi} \int_{-\infty}^{\infty} e^{is(E_0-E)} e^{-R\Sigma(s)} ds \tag{11}$$

with

$$\Sigma(s) = \frac{1}{\lambda_i} - \int_0^{\infty} K(T) e^{-isT} dT \tag{12}$$

where s is an integration variable without physical significance.

To determine the original (intrinsic) XPS spectrum $F(E,\Omega)$, a rigorous solution to Eq. (10) has been found [22]:

$$F(E,\Omega) = \frac{1}{P_1}\left[J(E,\Omega) - \frac{1}{2\pi}\int dE' J(E',\Omega) \int ds e^{-is(E-E')}\left(1 - \frac{P_1}{P(s)}\right)\right] \tag{13}$$

where

$$P(s) = \int f(z) e^{(-z/\cos\theta)\Sigma(s)} dz \tag{14}$$

with

$$P_1 = \int_0^{\infty} f(z) e^{-z/\lambda\cos\theta} dz \tag{15}$$

Since $P_1 = \lim_{s\to\pm\infty} P(s)$ and $1 - P_1/P(s) \to 0$ for $s \to \infty$ it follows that the function $1 - P_1/P(s)$ is suitable for discrete Fourier transformation [74]. Then the integral over s in Eq. (13) may be evaluated numerically by fast Fourier transformation. The remaining integral over E' and the integral over z may be evaluated by standard numerical methods. In this way, the original excitation spectrum corrected for inelastically scattered electrons $F(E,\Omega)$ is determined. Eq. (13) may be used to determine either $F(E,\Omega)$ if $f(z)$ is known (e.g. for a pure homogeneous sample) or it may be used to determine the in-depth concentration profile $f(z)$ if $F(E,\Omega)$ is known. Considerable information on $f(z)$ may be found even if $F(E,\Omega)$ is not known because, in general, one may always use the fact that $F(E,\Omega) \sim 0$ for all energies more than ~30 eV below the peak energy where the intrinsic excitations are negligible. For certain classes of atom depth distributions, part of the integration in Eqs. (14) and (15) may be done analytically [22]. In Section 5 we will consider some practical examples of application of Eqs. (10) and (13). First we shall however discuss the inelastic-scattering cross-section $K(E,T)$ which is needed to evaluate the above expressions.

3.2. Inelastic electron scattering cross-sections

The formulas for $J(E,\Omega)$ and $F(E,\Omega)$ involve $\Sigma(s)$ which depends on the inelastic-scattering cross-section $K(E,T)$. This quantity may be calculated from the dielectric function of the solid (by Eq. (2)). An alternative widely used technique is to determine $\lambda(E)K(E,T)$ experimentally by analysis of REELS [51,52] and software to do this analysis is also available [75]. These and related methods have been applied to systematic studies for a number of solids in a wide energy range [21,52–54,76,77]. We shall not review details of these methods here.

Table 1
Parameters for the Universal cross-sections, from [54].

Class of materials	B [eV^2]	B^N [eV^2][a]	C [eV^2]	D [eV^2]
Universal cross-section				
Metals and their oxides	2866	3286	1643	–
Three-parameter Universal cross-section				
Polymers	434	396	551	436
Silicon dioxide	325	299	542	275
Silicon	132	131	325	96
Germanium	73	93	260	62
Aluminum	16.5	21.4	230	4.5
REELS cross-section for transition metals and their oxides[b]				
Fit to Universal cross-section (Eq. (16))	760	1100	550	–
Fit to three-parameter Universal cross-section (Eq. (17))	4210	4645	1000	13300

[a] B^N is the value of B for which the cross-section is normalized. Some of the cross-sections are plotted in Fig. 7.
[b] The REELS cross-sections were determined from analysis of REELS spectra of Fe, Pd, Ti, Cu, Ag, and Au recorded at 2000 eV primary electron energy [54]. Note that although these cross-sections are determined from experiment, they are expected to overemphasize the influence of surface excitations. This is the reason why their maxima are at lower energy compared to the Universal cross-section which neglects surface excitations (see Fig. 7).

3.2.1. Universality classes of cross-sections

The concept of a Universal cross-section is an important step for practical modeling of the energy loss in XPS. This is so because for practical application of the algorithms in this section, it is essential to have general methods for fast and easy calculations of the probability for energy loss of electrons at any energy as they move in solids of general and non-uniform composition. The Universal cross-sections that was introduced in 1987 [53] was based on the observation that in general, the product $\lambda(E)K(E,T)$ depends strongly on T, moderately on the specific solid, and only weakly on E. Universal cross-sections will not account for the finer details but these are actually less important in this context, because the details in the energy spectra will be smeared out in measured spectra due in part to convolution with the intrinsic peak width and in part to multiple scattering. In the light of extensive and systematic experimental investigations of their validity, a critical discussion of the Universal cross-sections was given in 1997 [54]. The conclusions of this are as follows:

For most metals, their oxides, and alloys, the Universal cross-section

$$\lambda(E)K(E,T) = \frac{BT}{(C+T^2)^2} \tag{16}$$

with $C = 1643\,\text{eV}^2$ and $B \cong 3000\,\text{eV}^2$ applies with reasonable accuracy. The cross-section is normalized to unit area for $B = 2C = 3286\,\text{eV}^2$. This cross-section has successfully been applied in experimental studies of many systems (including metals, alloys, and metal-oxides).

The value $C = 1643\,\text{eV}^2$ was determined by a fit to cross-sections from a dielectric-response calculation [53] that neglected surface excitations. As seen in Table 1, a fit of Eq. (16) to cross-sections determined from experimental REELS spectra gives $C = 550\,\text{eV}^2$ and the maximum in the corresponding cross-section is at ~14 eV rather than at ~25 eV (see Fig. 7). This difference is due to surface excitations which are exaggerated in REELS where the electron passes the surface region twice compared to XPS where it passes the surface region only once and the best description of the average cross-section might be obtained with C somewhere in between these two values. It is interesting to note that Seah [78] found that the *ratio* of experimental XPS peaks from homogeneous samples, analyzed with the Universal cross-section was rather independent of the applied C value [78].

For solids (like Al) with a narrow plasmon structure, the cross-sections cannot be described well by a function with two parameters. For these solids, the main characteristics of the cross-section can be described well by the Three-parameter Universal cross-section [54]

$$\lambda(E)K(E,T) = \frac{BT}{(C-T^2)^2 + DT^2} \tag{17}$$

where the three parameters B, C, and D have been determined for different classes of materials (e.g. polymers, semiconductors, and free-electron-like solids [54] (see Table 1 and Fig. 7). This cross-section is particularly useful for solids with a narrow distribution of energy loss such as Al, Si, SiO_2, Ge GeO_2, and polymer films.

It was found [54] that the Universal cross-section, Eq. (16) is quite accurate for solids when their cross-section has a full width at half maximum >20 eV. For solids with a cross-section width of 10–15 eV, the Universal cross-section is still fairly good for the description of the far-peak region (>30 eV from the peak energy) but it is less accurate in accounting for the near-peak region (<10 eV from the peak energy). For solids with a cross-section width <5 eV (e.g. Al, Si), the Three-parameter Universal cross-section, Eq. (17)

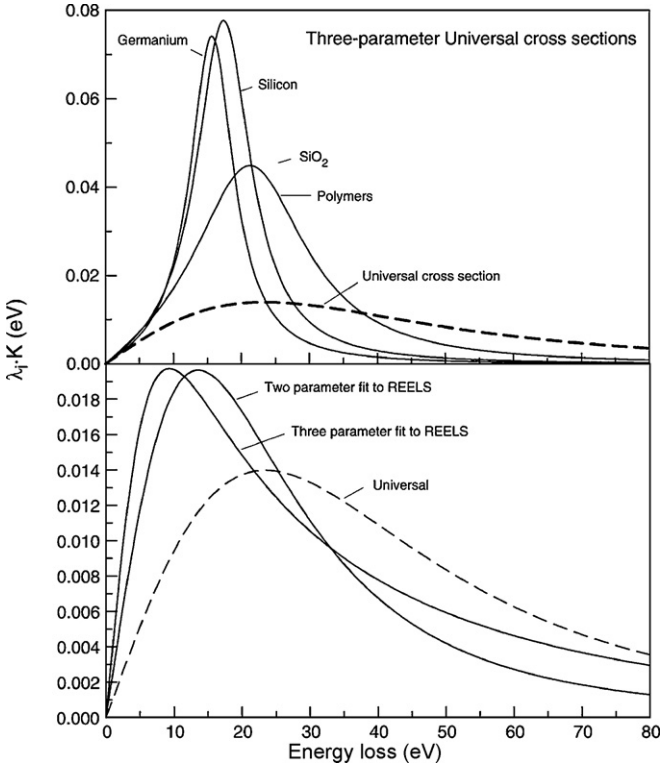

Fig. 7. Cross-sections for different classes of materials. See Table 1, from [54].

is always significantly more accurate than the Universal cross-section.

The basic idea behind the Universal cross-section is that the material and energy dependence of $K(E,T)$ is separated in the factor $\lambda(E)$. For practical application with the formulas in Section 3, the absolute cross-section $K(E,T)$ is found from Eqs. (16) or (17) by division with λ. There is plenty of knowledge available on $\lambda(E)$ [3–6] and for a general solid it can be estimated by, e.g. the TPP-2M formula [4].

3.3. Extrinsic excitations in the two-step model

There is a strong correlation between the intensity of a given spectral energy region and the depth where these electrons were emitted [23]. For example, the elastic peak intensity (Eq. (1)) depends strongly on the atomic concentration at depths <1λ but is rather independent of the concentration at depths exceeding 3λ. On the other hand, the spectral intensity 100 eV below the peak energy depends strongly on electrons excited from atoms at 3–4λ depth but depends much less on the atomic concentration for depths <1λ. Different energy regions of the spectrum thus carry information on the atomic concentration at different depths. To facilitate one's thinking while doing practical spectral analysis, it is useful, together with Fig. 1, to have a rough model in mind. If the typical energy loss in a single-scattering event is denoted by δE, then the intensity in an energy range ΔE below the peak energy is primarily determined by the distribution of electron emitters within the outermost depth range:

$$R = \frac{\Delta E}{\delta E}\lambda \tag{18}$$

where typically $\delta E \sim$ 15–30 eV depending on the solid (see Fig. 7). With ΔE = 100 eV, one gets $R \sim$ 4–7λ. The spectrum in an energy range up to ~100 eV from the peak energy is then primarily determined by the composition within the outermost 5λ and the contribution from electrons excited at larger depths will be small. Since the cross-section for electron energy loss in solids is in general a wide function of energy loss (see Fig. 7), there is considerable overlap in the intensity contributions at a given spectral energy from electrons excited at different depths. For this reason, there is not a direct one-to-one correspondence between depth of origin and energy loss. For a typical case, it has been shown [23] that 100 eV below the peak energy, the spectral intensity contribution from electrons that are excited at all different depths between 0.73λ and 5.1λ vary by only a factor of two. It is this smearing effect that primarily determines the practical accuracy for depth profiling using peak-shape analysis. However, as shown in [23], this smearing effect has very little influence on the accuracy of the amount of substance (or the average surface concentration) in the surface region determined from the inelastically scattered electrons by analyzing the peak-shape.

For accurate calculation of energy spectra with Eq. (10), the change in energy distribution as a function of path length R traveled is given by Eqs. (11) and (12). These expressions look simple, but are rather complex to evaluate, and numerical methods are required to calculate the energy loss function G. As shall be seen in Section 4, algorithms for *removal* of the inelastic background from measured spectra with Eq. (13) can be effectively solved numerically by means of discrete Fourier transformation using a fast Fourier transformation algorithm. This approach will however not work for numerical evaluation of Eqs. (11)–(12). The reason is that, as discussed above, for a general depth distribution $f(z)$, both small and large path lengths $R = z/\cos\theta$ will contribute to the spectrum. For larger path lengths, the electron energy distribution function G will have appreciable intensity over an energy range of several hundred electron-volts. The discrete approximation of this function, given by a discrete Fourier transforms, therefore fails [79]. Other numerical methods have therefore been applied to evaluate the energy distribution spectrum. Two such methods are discussed in the following two subsections.

3.3.1. Expansion method

By a Taylor expansion of Eq. (11) in multiple scattering terms, one obtains formulas for numerical evaluation of the energy distribution function [55,56]

$$\begin{aligned} G(E_0,R;E) = \frac{1}{2\pi}\int_{-\infty}^{\infty} e^{is(E_0-E)}e^{-R\Sigma(s)}ds = e^{-R/\lambda}\{\delta(E_0-E) + RK(E_0-E) \\ + \frac{R^2}{2}\int dTK(T)K(E_0-E-T) + \frac{R^3}{6}\int dTK(T) \\ \times \int dT'K(T')K(E_0-E-T-T') + \ldots\} \end{aligned} \tag{19}$$

The number of expansion terms needed to get sufficient accuracy depends on the energy range studied. The four terms in Eq. (19) correspond to unscattered, single, double, and triple scattered electrons, respectively. The typical energy loss in a single-scattering event is 15–30 eV (see Fig. 7) and correspondingly the four terms are fully sufficient to describe the energy spectrum in a ~50 eV energy loss range below a peak. For accurate description of wider energy spectra, expansion to higher orders is required. The convolution integrals in Eq. (18) are most effectively evaluated by multiplying the discrete Fourier transformed functions followed by an inverse Fourier transformation, and numerical calculations to say 10th order scattering are then completed within a fraction of a second.

3.3.2. Layer doubling method

A convolution technique [80] was used early on to simulate XPS spectra [21,81]. Because of the basic principle of this technique, it was given the name *layer doubling method* [82]. Thus, it relies on the fact that the probability that an electron has lost energy T after traveling the distance $2R$ may be evaluated by convoluting the distribution of electrons that have lost energy $T-T'$ over a distance R with the distribution of electrons that have lost energy T' over the distance R. With the present notation, this gives [82]:

$$G(E_0,2R;E) = \int_0^{E_0-E} G(E_0,R;E-T)G(E_0,R;E+T)dT \tag{20}$$

For sufficiently small R, denoted by r, with $r \sim 0.01\lambda$, the chance for multiple electron scattering can safely be neglected and the probability for energy loss T is $rK(E_0,T)$, while the probability that the electron remains unscattered is $(1-r/\lambda)$, i.e.

$$G(E_0,r;E) = \left(1-\frac{r}{\lambda}\right)\delta(E_0-E) + rK(E_0,T) \tag{21}$$

Inserting Eq. (21) into Eq. (20) gives

$$\begin{aligned} G(E_0,2r;E) = \left(1-\frac{r}{\lambda}\right)^2\delta(E_0-E) + 2\left(1-\frac{r}{\lambda}\right)rK(E_0,T) \\ + \int_0^{E_0-E} r^2K(E_0,T-T')K(E_0,T')dT' \end{aligned} \tag{22}$$

By repeated use of this procedure, the function G may be evaluated for any depth, and after n convolutions:

$$G(E_0,2^nr;E) = \left(1-\frac{r}{\lambda}\right)^{2^n}\delta(E_0-E) + g_n(E_0-E) \tag{23}$$

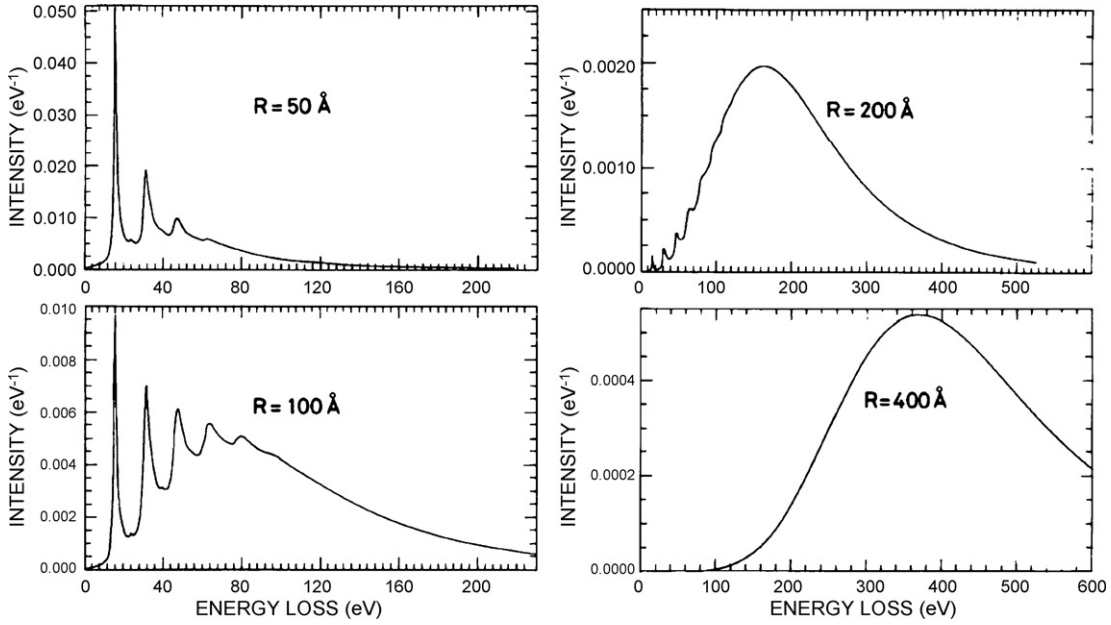

Fig. 8. Energy distribution of a single electron of initial energy 1167 eV after having traveled the distance R in Al, from [81].

where

$$g_n(T) = 2\left(1 - \frac{r}{\lambda}\right)^{2^{n-1}} g_{n-1}(T) + \int_0^T g_{n-1}(T')g_{n-1}(T - T')dT' \quad (24)$$

with $g_0(T) = rK(E_0,T)$

This algorithm (as well as the Landau formula (Eqs. (11)–(12)) is valid when the total energy loss is sufficiently small compared with the initial electron energy E_0 that the dependence of the cross-section on E_0 can be neglected. Fig. 8 shows spectra calculated with this procedure [81] for 1167 eV electrons that have traveled various distances in Al for which the plasmon excitation energy is $\delta E = 15.6$ eV and $\lambda = 21.5$ Å. The peaks corresponding to multiple plasmon excitations are clearly seen and these structures are smeared out for larger R. From Eq. (18) we find an estimate for the mean energy loss $\Delta E = 36$, 73, 145, and 290 eV for $R = 50$, 100, 200, and 400 Å, respectively, which are in rough agreement with the distributions in Fig. 8.

3.4. Validity of the two-step model

In the past two decades, the two-step model used together with the Universal cross-sections has been applied with considerable success to describe the changes in peak intensity and extrinsic electron energy distribution caused by variations in the atom depth distribution. Numerous systems have been studied a few of which are described in Section 4. Here we take two examples. Fig. 9 shows spectra from samples where various amounts of ZnO are deposited on a SiO_2 substrate, and on an oxidized Al surface, respectively [83]. The Zn2p, Zn LMM, Si KLL, and Al KLL spectra were acquired sequentially (denoted 1, 2, 3, 4) after increasing amounts of ZnO were

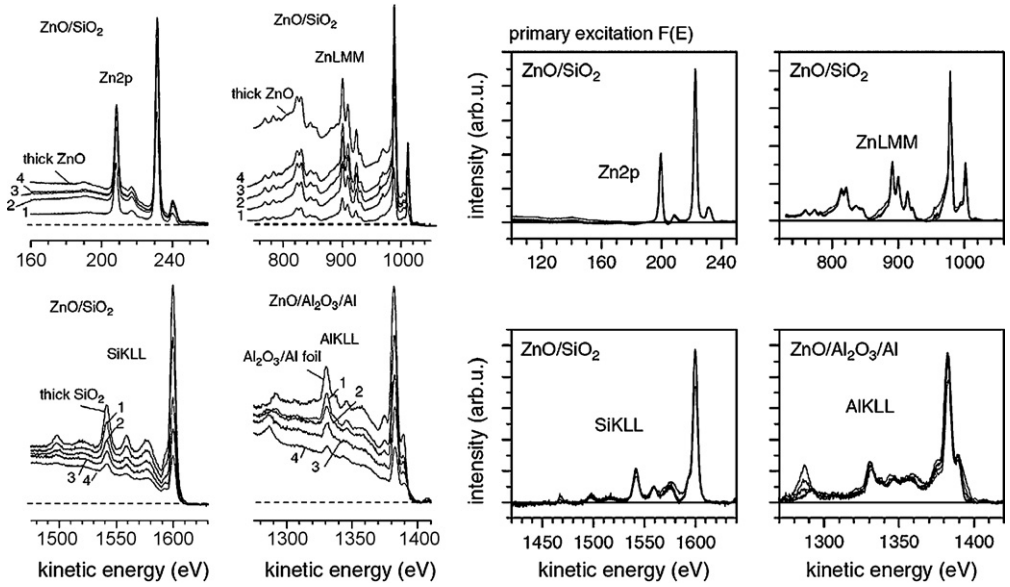

Fig. 9. Left panel: spectra for the Ni2p, Zn LMM, Si KLL, and Al KLL peaks measured for increasing depositions of ZnO. Right panel shows the same spectra after being corrected according to the two-step model, i.e. by Eq. (13), from [83].

deposited. With increasing overlayer thickness, the energy spectra are strongly affected due to the corresponding change in multiple inelastic-scattering processes that the Si KLL and Al KLL electrons will undergo on their way out. This is seen as a gradual decrease in peak intensity and an increase in the background signal below the peak energy. A similar phenomenon is seen for the Zn2p and Zn LMM peaks, where both the peak and the background intensity increase as the Zn layer thickness increases (see also Fig. 1) In the right-hand panel, these spectra have been corrected for the second step in the two-step model, i.e. the effects of the inelastic-scattering processes are removed with Eq. (13) while $f(z)$ in Eqs. (14) and (15) is varied until a good account of the extrinsic electrons is achieved (see Section 4 for details of how this is done; the determined $f(z)$ are shown in Fig. 19 below). The resulting $F(E)$ spectrum is the excitation spectrum in step 1, i.e. the intrinsic spectrum at the point of excitation in the solid. To the extent that the two-step model is valid, the spectra should be identical. As can be seen, the spectra are almost identical over the 1–200 eV energy range. Note that the $F(E)$ spectra are determined on an absolute scale and have not been scaled. Using synchrotron radiation, it was shown [84] that the two-step model also gives approximately identical Au4f intrinsic spectra (from a gold foil) for photon energies of 300–1600 eV although observed small deviations could be ascribed to surface excitations which will be more pronounced at lower energies but which are not included in the two-step model. If the angle of emission is varied, one might get larger deviations (see Fig. 5) but usually quantitative XPS is done with the analyzer in a fixed position. A similar example is shown in Fig. 10 where a thin layer of Au was evaporated onto the surface of a Ni sample. This was followed by evaporation of increasing amounts of Ni on top. This results in very large changes in both the peak intensity and the energy distribution of extrinsic electrons. After correction for extrinsic electrons by Eq. (13), varying $f(z)$ in Eqs. (14)–(15), the intrinsic spectrum is determined [22]. They are all practically identical.

These two examples, as well as numerous other examples show that the *variations* in intensity and peak-shape caused by variations in atom concentration with depth are quite well described by the two-step model.

3.5. Peak intensity

If one is only interested in the peak intensity, the detailed distribution of energy loss is not important and further simplifications of the model may be made. The measured intensity depends on the instrumental efficiency D_{instr} which describes the characteristics of the X-ray source and the electron energy analyzer. This can be separated into two factors, $D_{instr} = D\,T(E)$, where $T(E)$ is the energy dependent part (often called the analyzer transmission function), and D the energy independent part. Procedures to determine $T(E)$ have been developed [85] and in general $T(E)$ is a smooth function of E and is for hemispherical analyzers often approximated by E^{-m} with $m = 0.7$ (in general $0.5 < m < 1$, and m depends on E and the pass energy of the spectrometer). If one uses standard spectra in the analysis, this correction is not essential. Consider now photoelectrons excited from atoms of type A resulting in a peak centered at energy E_A with peak intensity $I_A^{measured}$. Correction of the measured intensities by the energy dependent part of the detector efficiency results in $I_A = I_A^{measured}/T(E_A)$. For the situation where atoms A are in a thin layer of thickness dz at a depth z in a solid and assuming that the X-ray irradiated surface area is larger than the area A_0 from which photoelectrons are accepted into the analyzer, the intensity from the layer is

$$I_A(z) = \left[D\frac{A_0}{\cos\theta}\right]\left[\frac{d\sigma_A(h\nu)}{d\Omega}W_A(\gamma,\beta_A)\right][N_A CF_A(z,\theta,E_A)] \times \exp\left(\frac{-z}{(\lambda\cos\theta)}\right)dz\Delta\Omega \quad (25)$$

where $\Delta\Omega$ is the solid acceptance angle of the analyzer, $\sigma_A(h\nu)$ the photoionization cross-section for the particular core level in atom A for photons of energy $h\nu$, N_A the atomic density of A atoms, γ the angle between the incident x-ray beam and the electron detector, and $W_A(\gamma,\beta_A) = 1 + 1/2\beta_A(3/2\sin^2(\gamma) - 1)$ describes the anisotropy of the photoemission. σ_A and the asymmetry parameter β_A for the core level A can be taken from theoretical or experimental tables [86–89]. For $\gamma = 54.7^\circ$, W_A is independent of β_A and many spectrometers are designed to operate close to this geometry.

The factor $CF_A(z,\theta,E_A)$ accounts for the effects of elastic electron scattering [90]. By definition, $CF = 1$ when elastic scattering is negligible, i.e. when the electron moves along a straight line from the point of excitation to the detector entrance. This factor was introduced [90] as a practical way to account for elastic electron scattering effects. From extensive Monte Carlo simulations, it was found that CF can be expressed in a simple parameterization, which becomes particularly simple for the experimental geometry where $\theta < 30^\circ$ and $45^\circ < \gamma < 65^\circ$, which is typical for most instruments. For this geometry, the expression was found [91]

$$CF(z,\theta) \cong \exp(-0.157764\tau - 1.25132) + \exp(-0.0562417\tau^2 + 0.00698849\tau - 0.201962) \quad (26)$$

where $\tau = z(\lambda + \lambda_{tr})/(\lambda\lambda_{tr})$, λ_{tr} being the transport mean free-path. Thus CF is independent of θ for $\theta < 30^\circ$. For larger values of θ, a more general parameterized expression was found [91]. For those cases where the majority of the detected photoelectrons come from atoms at depths $<1-2\lambda$, CF is generally a small correction ($\sim$0.9–1.1). For homogeneous materials, $CF \sim 1$ because electrons

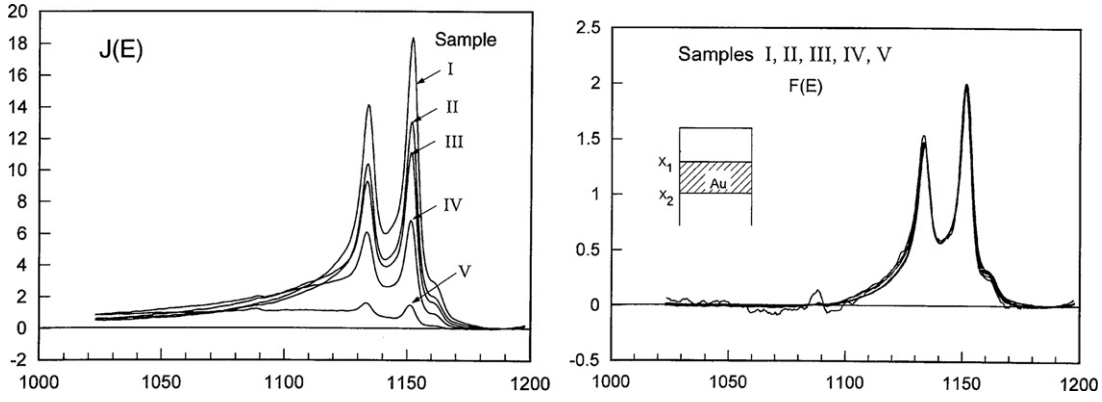

Fig. 10. Left panel shows Au4d spectra measured from a ~1 nm thick gold layer on a Ni surface (I) and after being buried at increasingly larger depths (II–V) by consecutive evaporation of nickel on top. Right panel shows the same spectra after being corrected according to the two-step model, i.e. by Eq. (13), from [23].

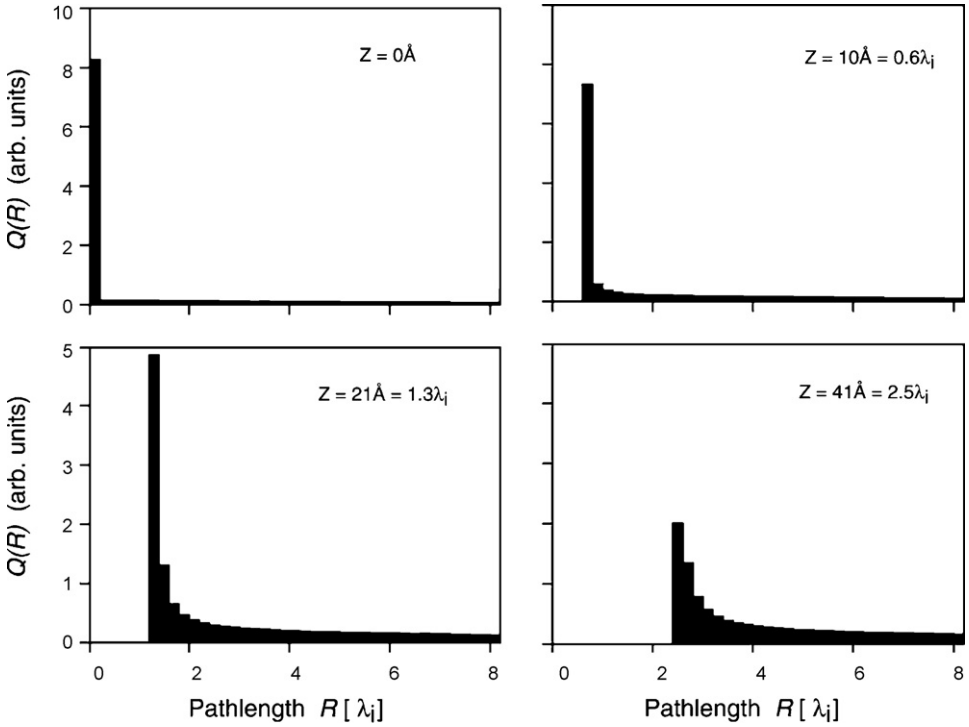

Fig. 11. Monte Carlo calculation of the distribution of path lengths $Q(R)$ traveled by Au4d electrons (of 1140 eV energy) before they escape from the surface after being excited at depth z in a Ni-solid. If there were no elastic scattering, all electrons would escape with $R = z$ and $Q(R) \sim \delta(z - R)$, from [93].

from the shallower layers dominate the measured peak intensity. In situations where all the photoelectrons come from depths >2λ (e.g. a substrate with a thick overlayer), the *CF* correction can be substantial. Thus, the effect of elastic scattering is more pronounced for samples where most atoms of interest are distributed at large depths. This is also evident from Fig. 11 which shows Monte Carlo calculations of the distribution of path lengths $Q(R)$ traveled by Au4d electrons (of 1140 eV kinetic energy) before they escape along the surface normal after being excited at depth z in a Ni-solid [92,93]. It is evident that when the electrons are excited at a depth of 41 Å (equivalent to 2.5λ), a typical electron has traveled a distance that is substantially larger than that corresponding to a straight line trajectory. Fig. 11 also shows that for depths <1λ, this redistribution of path lengths caused by elastic electron scattering is small. For atom distributions where $CF \sim 1$, Eq. (25) becomes Eq. (1)

Here we have described the effect of elastic electron scattering by the *CF* factor. An alternative procedure is to replace λ by an effective attenuation length. This attenuation length will then depend on both the depth z and the experimental geometry [94]. Effective attenuation lengths have been studied in detail by Monte Carlo simulations [95]. It should be noted that the formulation presented in Sections 3.1 and 4 neglect the effect of elastic electron scattering. The exact effect of elastic scattering is complex to describe but in essence it will change the effective depth scale and this can approximately be described by replacing λ by an effective attenuation length.

3.5.1. Surface excitation parameter

In Section 2.1.2 it was shown that the presence of the surface may cause considerable changes in the energy loss spectrum. If one is not interested in the detailed change in peak-shape but only in the change in peak intensity caused by the surface, this can conveniently be described by a simple parameter where the surface excitation is expressed as a probability, namely the surface excitation parameter (SEP) $P_S(E,\theta)$ which is originally defined as "the average number of excitations an electron of energy E undergoes when it crosses the surface once at an angle θ with respect to the surface normal" [96,11,14]. It has been pointed out [16] that there are several ambiguities with this definition; such as the decrease of the bulk inelastic cross-section close to the surface while the surface excitations increase. The effect of this is not included in this definition and another ill-defined quantity is the exact extension of the effective surface region. That implies that P_S obtained within this definition cannot be directly used as a correction factor to the elastic peak intensity (on the form $\exp(-P_S(E,\theta))$). This complication is overcome by redefining the surface excitation parameter as the "change in excitation probability, for an electron caused by the presence of the surface in comparison with the excitations suffered by an electron that travels the same distance in an infinite solid" [13,16]. This definition gives a transparent meaning of P_S which can then readily be applied in practical surface analysis and Eq. (1) is changed into

$$I(z) = I_0 e^{-z/(\lambda \cos\theta)} e^{-P_S} \tag{27}$$

Fig. 12 shows examples of P_S calculations for different materials, energies and geometries using a software package QUEELS-$\epsilon(k,\omega)$-REELS [72] which is based on the semi-classical dielectric-response model for REELS [46,67] which is similar to the model described in Section 2.1, for XPS. In both cases, the only input in the calculations is the dielectric function of the medium.

An approximate parameterization of the dependence on energy and angle was found [11]

$$P_S(E,\theta) = \frac{1}{0.173 a E^{1/2} \cos\theta + 1} \tag{28}$$

where a is a material dependent parameter, E is in eV and the factor 0.173 is in $eV^{-1/2}$. In Fig. 12 the lines denoted Oswald are fits by Eq. (28). Determined a values for selected materials are given in Table 2.

Most published P_S values have been based on analysis of spectra from a REELS geometry [11,13,97–100]. However due to the effect of the core-hole, one expects P_S to be different for XPS. The extent

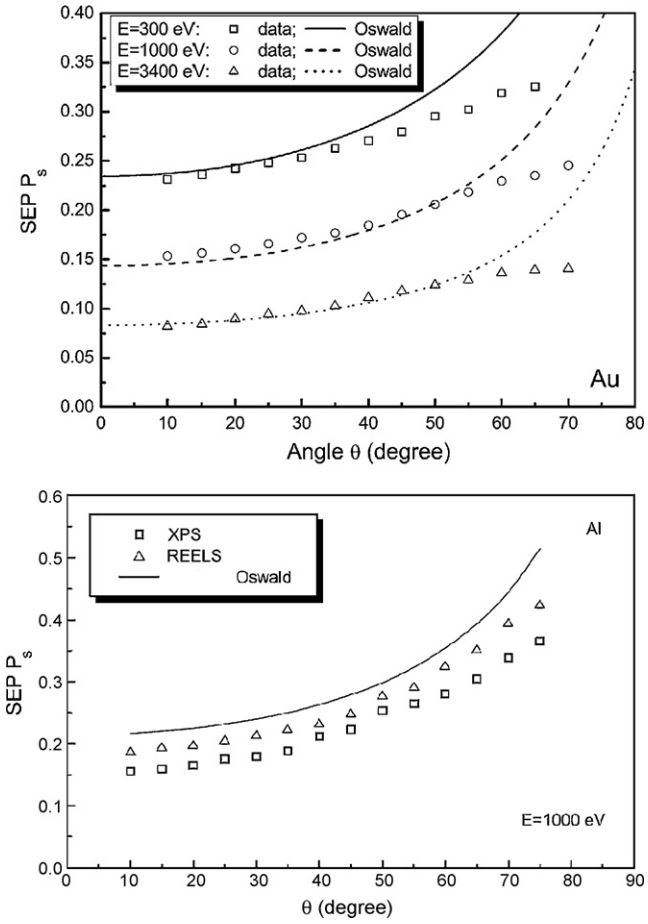

Fig. 12. Upper panel: angular distribution of the SEP P_S for Au and energies of 300, 1000 and 3400 eV as well as the fits obtained by Eq. (28) (with $a = 1.09$), from [100]. Lower panel: P_S for Al at 1000 eV □: theoretical data obtained from XPS spectra; △: theoretical data obtained from REELS spectra. Solid line [11] from experimental REELS: Eq. (28), from [100] Note that the values were determined for a REELS geometry and may not apply for XPS due to the influence of the core-hole.

of this difference was studied [101] by the model in Section 2.1 and an example for Al at 1000 eV is shown in Fig. 12 as a function of the exit angle. Also shown are results found from theoretical REELS spectra [12] as well as the experimental REELS results taken from [11].

The agreement between theoretical and experimental REELS determined values is quite good. Considering the points obtained from the theoretical XPS calculation, one observes that P_S for XPS is consistently smaller by ~5–10% for Al compared to REELS. This effect is due to the presence of the core-hole which produces an attractive potential to the photoelectron and increases the energy losses in the bulk while the surface loss remains almost unchanged. This systematic decrease of 5–10% is however not very large in comparison to observed variations [11] in the surface excitation probability due to surface roughness.

It must be emphasized that P_S in these XPS simulations were determined using the definition of P_S in [96,11,14] rather than the definition in [13,16]. Consequently one should be cautious about using the values for P_S, given in this section and in Fig. 12, to correct XPS peak intensities with Eq. (27). Thus, more investigations are required in order to determine the correct values for P_S taking the influence of the core-hole into account and using that definition of P_S for which Eq. (27) is valid.

Table 2
Values a in Eq. (28) for selected materials (PE is polyethylene). Note that the values were determined for a REELS geometry and may not apply for XPS, from [12,16].

Medium	Si	Au	Cu	Fe	Pd	Ti	SiO_2	TiO_2	PE
a	0.72	1.09	1.23	1.87	1.40	1.78	3.66	2.14	2.29

4. Evaluation of XPS energy spectra

There are two different but equivalent approaches for quantitative nano-composition analysis within the two-step model. Either one starts with an intrinsic spectrum, and calculates the changes due to extrinsic energy loss and compares the resulting spectrum on an absolute scale to the measured XPS. The extrinsic contributions will vary with the depth distribution of photoemitting atoms which is thus determined.

In the other approach, one corrects the measured XPS spectrum for the extrinsic contributions and determines the intrinsic XPS spectrum. This analysis can be done without a reference spectrum; however the accuracy is enhanced when it is compared to a standard intrinsic spectrum determined from analysis of XPS from a sample with known depth distribution. Usually (but not necessarily) a sample with homogeneous depth distribution is used for this purpose. Again the depth distribution of atoms is varied until a good match between the two intrinsic spectra is obtained.

4.1. Determine the total (extrinsic plus intrinsic) spectrum

Calculation of the spectrum $J(E,\Omega)$ from Eq. (10) requires that the depth concentration distribution of atoms $f(z)$ and the initial excitation energy spectrum $F(E,\Omega)$ are known. $F(E,\Omega)$ may, e.g. be determined from analysis, with Eq. (30) below, of a spectrum from a sample with a known in-depth distribution, for example the spectrum $J_h(E,\Omega)$ from a pure homogeneous sample. It can also be both a practical and computational advantage to reformulate Eq. (10) such that the spectrum $J_h(E,\Omega)$ enters directly into the formalism [79]. The energy distribution G of electrons, as a function of the path length traveled in the solid, is calculated by one of the methods described in Section 3.3. The resulting model spectrum is overlaid with the measured spectrum and the absolute intensity and the peak-shape compared. This is done for different assumed in-depth concentration profiles $f(z)$. When a good agreement between the model spectrum and experiment is found, the corresponding $f(z)$ is the true in-depth distribution concentration profile of atoms. This method was applied in several cases see, e.g. [17,40,79,102–110] (see also Section 5).

4.2. Determine the intrinsic spectrum

If the analyzed peaks do not overlap in energy, it is often preferred to apply Eq. (13) which removes the extrinsic electrons and determines the undistorted (intrinsic) spectrum. This has the advantage that the intrinsic spectrum does not necessarily need to be known. This method was applied in several cases see, e.g. [17,21,23,27,55,56,83,103,108–130] (see also Section 5).

4.2.1. General inversion formula

A rigorous and general solution for $F(E,\Omega)$ is given by Eq. (13). However analytic expressions have been found for certain classes of depth profiles $f(z)$, and these are now described.

4.2.2. Homogeneous and exponential depth profiles

When the distribution of atoms is either constant or exponentially varying with depth, i.e.

$$f(z) = ce^{-z/L} \tag{29}$$

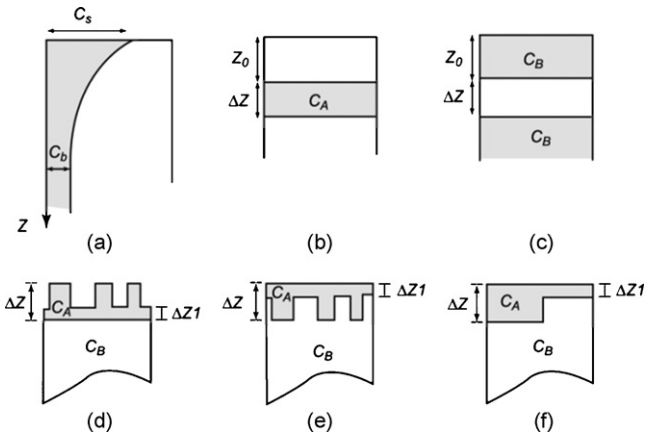

Fig. 13. Definition of parameters for some in-depth profiles. Note that the structures in (d), (e), and (f) give identical spectra.

there is an exact solution to the inversion problem [81]:

$$F(E,\Omega)=\frac{L+\lambda\cos\theta}{c\lambda L\cos\theta}\left[J(E,\Omega)-\frac{\lambda L}{L+\lambda\cos\theta}\int_E^\infty dE' J(E',\Omega)K(E'-E)\right] \tag{30}$$

For a homogeneous depth distribution, $L\to\infty$ and [18]

$$F(E,\Omega)=\frac{1}{c\lambda\cos\theta}\left[J(E,\Omega)-\lambda\int_E^\infty dE' J(E',\Omega)K(E'-E)\right] \tag{31}$$

4.2.3. General exponential depth profiles

If the exponential in-depth profile is such that the concentration is not vanishing for large depths but approaches a constant concentration C_b in the bulk (see Fig. 13a) then

$$f(z)=(C_s-C_b)e^{-z/L}+C_b \tag{32}$$

and analytic expressions for P_1 and $P(s)$ can be found

$$P_1=C_b\lambda\cos\theta+(C_s-C_b)\frac{L\lambda\cos\theta}{L+\lambda\cos\theta} \tag{33}$$

and

$$P(s)=C_b\frac{\cos\theta}{\Sigma(s)}+(C_s-C_b)\frac{L\cos\theta}{L\Sigma(s)+\cos\theta} \tag{34}$$

which are then used in Eq. (13). Note that although formulas (32)–(34) have been implemented in the QUASES software [58] since Version 3.1 many years ago, this is the first time these expressions are published in a scientific journal.

4.2.4. Delta layer profile

When N atoms are all at depth z_0

$$f(z)=N\delta(z-z_0) \tag{35}$$

and one obtains the exact expressions [22]

$$P_1=Ne^{-z_0/(\lambda\cos\theta)} \tag{36}$$

and

$$P(s)=Ne^{-z_0\Sigma(s)/\cos\theta} \tag{37}$$

4.2.5. Box-shaped profiles (overlayer, substrate and sandwich)

Overlayer and substrate profiles are special cases of the general sandwich profile shown in Fig. 13b and c. The atoms of type A in the sandwich layer have the concentration profile

$$f_A(z)=\begin{cases}0 & \text{for } 0<z<z_0\\ C_A & \text{for } z_0<z<z_0+\Delta z\\ 0 & \text{for } z_0+\Delta z<z\end{cases} \tag{38}$$

and then [22]

$$P_1=C_A\lambda\cos\theta e^{-z_0/(\lambda\cos\theta)}[1-e^{-\Delta z/(\lambda\cos\theta)}] \tag{39}$$

and

$$P(s)=C_A\frac{\cos\theta}{\Sigma(s)}e^{-z_0\Sigma(s)/\cos\theta}[1-e^{-\Delta z\Sigma(s)/\cos\theta}] \tag{40}$$

The matrix material that surrounds the sandwich layer consists of type B atoms with the atom concentration as a function of depth z given by

$$f_B(z)=\begin{cases}C_B & \text{for } 0<z<z_0\\ 0 & \text{for } z_0<z<z_0+\Delta z\\ C_B & \text{for } z_0+\Delta z<z\end{cases} \tag{41}$$

and then [22]

$$P_1=C_B\lambda\cos\theta\{1-e^{-z_0/(\lambda\cos\theta)}[1-e^{-\Delta z/(\lambda\cos\theta)}]\} \tag{42}$$

and

$$P(s)=C_B\frac{\cos\theta}{\Sigma(s)}\{1-e^{-z_0\Sigma(s)/\cos\theta}[1-e^{-\Delta z\Sigma(s)/\cos\theta}]\} \tag{43}$$

Algorithms for analysis of spectra from atoms in an overlayer of thickness Δz and from atoms in a substrate covered with an overlayer of thickness Δz are obtained by setting $z_0=0$ in the above sets of equations.

4.2.6. Island structures

Here, a general island structure as in Fig. 13d, where atoms of type A cover the surface of a substrate of atoms of type B, is considered. In the general case, a layer of height Δz_1 covers the surface completely, and islands with mean height $\Delta z-\Delta z_1$ are formed on top. The spectrum from the structure in Fig. 13d is the same as the spectrum from Fig. 13e, which again is the same as the spectrum from the atom distribution shown in Fig. 13f (note that this is not true for very glancing emission angles where a shadowing effect may occur. It is therefore preferred to measure at normal or near normal emission angles (<45°) when such structures are studied). Denoting the fraction of the surface that is covered by islands by f_1, the atom concentration profile for the overlayer atoms is

$$f_A(z)=\begin{cases}C_A & \text{for } 0<z<\Delta z_1\\ f_1C_A & \text{for } \Delta z_1<z<\Delta z\\ 0 & \text{for } \Delta z<z\end{cases} \tag{44}$$

and then [22]

$$P_1=C_A\lambda\cos\theta\{1-(1-f_1)e^{-\Delta z_1/(\lambda\cos\theta)}-f_1e^{-\Delta z/(\lambda\cos\theta)}\} \tag{45}$$

and

$$P(s)=C_A\frac{\cos\theta}{\Sigma(s)}\{1-(1-f_1)e^{-\Delta z_1\Sigma(s)/\cos\theta}-f_1e^{-\Delta z\Sigma(s)/\cos\theta}\} \tag{46}$$

For the substrate atoms of type B, the atom concentration as a function of depth z is

$$f_B(z)=\begin{cases}0 & \text{for } 0<z<\Delta z_1\\ (1-f_1)C_B & \text{for } \Delta z_1<z<\Delta z\\ C_B & \text{for } \Delta z<z\end{cases} \tag{47}$$

and then [22]

$$P_1=C_B\lambda\cos\theta\{(1-f_1)e^{-\Delta z_1/(\lambda\cos\theta)}+f_1e^{-\Delta z/(\lambda\cos\theta)}\} \tag{48}$$

and

$$P(s) = C_B \frac{\cos\theta}{\Sigma(s)}\{(1-f_1)e^{-\Delta z_1 \Sigma(s)/\cos\theta} + f_1 e^{-\Delta z \Sigma(s)/\cos\theta}\} \quad (49)$$

The situation where only a fraction of the surface is covered with islands is obtained with $\Delta z_1 = 0$. The general case where the surface structure consists of several types of islands with different height and surface coverage are obtained by generalization of the above formulas and are implemented in the QUASES software [58].

5. Applications of the formalism to non-destructive depth profiling

The accuracy and limitations of the formalism in Section 4 to quantitative nano-structure analysis was established about a decade ago in [23] from a detailed analysis of a range of model spectra and three sets of experiments. It was found that information on the concentration–depth profile in the surface region up to depths of 5λ is primarily contained in the spectral energy region up to ~100 eV below the peak energy and is essentially completely contained by the energy region up to ~200 eV below the peak. Analysis of a larger energy range than 100 eV does not add much to the information on the details of the structure in the outermost 5λ but gives the possibility to determine additional structural parameters that describe the composition at larger depths. In [23], the structural parameters that describe the chemical composition of the outermost 5–10λ of the solid were divided into primary and secondary parameters: the primary parameters are the three most important parameters needed to describe the main characteristics of the distribution of atoms; the secondary parameters are parameters, other than these three primary parameters, that describe the finer details of the depth distribution of atoms in the outermost 5–10λ of the surface region. The uncertainty in the determined three primary parameters is typically 5–10%. The uncertainty in the determined secondary parameters is typically $\gtrsim$35%. Different models of depth profiles can be distinguished when they differ significantly over a width of more than ~1/3λ at any depth $\lesssim$5λ. The uncertainty in the total determined amounts of atoms within the outermost 5λ (regardless of their depth distribution) is 5–10%. These uncertainties hold for situations when the peak can be isolated from overlapping peaks in an energy range from a few eV above to at least 50 eV below the peak energy. If this is not the case, analysis is still possible but the fitting procedure gets more involved and the accuracy may be worse.

In this section we will discuss only a few of the many published practical applications of the formalism in Section 4. The examples have been selected to illustrate the basics of both the potentials, the validity, and the limitations of the technique. First we discuss an example where it was used to determine the growth mechanism for deposited thin films. As we shall see, it is very easy to determine, e.g. whether the film forms a continuous layer on the substrate or if islands are formed. Since the technique is non-destructive and all information is found from analysis of a single spectrum, it is possible to do real-time analysis. Thus, it is easy to, e.g. follow the gradual redistribution of atoms caused by chemical reactions or diffusion during annealing. Much of the information determined with XPS peak-shape analysis is hard to get by other techniques. Thus, atomic force microscopy (AFM) and scanning tunneling microscopy (STM) are very powerful to determine the surface topography but they give limited information on the type of atoms and no information on what atoms are in the second, third and deeper layers. On the other hand, Rutherford backscattering spectrometry (RBS) and X-ray fluorescence (XRF) cannot provide detailed depth information on the nano-scale, but they are rather accurate in determining the total amount of atoms in the surface region. There are several papers in which this quantity was compared with the XPS results and a couple of these will be discussed below. In cases where comparison is possible, there is a good agreement between the techniques. In some cases deviations on the absolute scale have been found, while the agreement on the relative scale is very good. This is of course eliminated when local calibration is used, as is the usual practice. Another purpose of background subtraction is to simply isolate the peak for peak-area determination and for identification of the chemical states. The influence of background subtraction on the determined chemical state energy was studied, e.g. in [131]. Here we shall focus on application of inelastically scattered electrons for quantitative analysis of nano-structures.

To put the discussion in this section into a practical perspective, we add a brief remark on the angle-resolved XPS (ARXPS) method [132,133] which is another possible method to correct for the depth dependence of the intensity. This method relies on analysis of spectra of an XPS peak measured at two or more angles of emission. Since the attenuation of the peak varies with depth of origin of the electron-emitting atom, information on the depth distribution can be determined. While this method works well for very flat surfaces, it fails completely when the surface is quite rough or when tall nano-structured islands are formed on a flat surface because of the shadowing effect [134,135]. To correct for this, a-priori information on the morphology must be available [132,133]. The peak-shape analysis method does not have these limitations since all information is extracted from a single spectrum taken at a fixed angle of emission and, if this is chosen close to the surface normal, the shadowing effects are eliminated or minimized. Thus, the peak-shape analysis method always gives a "top-down" analysis in the spectrometer axis direction at the analyzed spot on the surface.

In [114], the mechanism for growth of Cu, Ag, Au and Pt metals on Si(1 1 1) was studied. The analysis procedure is shown in Fig. 14 taking Pt as an example. First, a reference intrinsic $F(E,\Omega)$ for Pt was determined by analysis of XPS of the Pt4d peak measured from a pure Pt foil using Eqs. (38)–(40) with $z_0 = 0$ Å and $\Delta z = \infty$. This was followed by analysis of Pt4d taken from the thin-film structure, after deposition of a certain amount of Pt on Si(1 1 1). This is done with assumed growth parameters which are varied until good agreement with the reference $F(E,\Omega)$ is obtained both with respect to intensity and shape. If it is assumed that the film covers the complete surface, the best overall agreement (see Fig. 14) is obtained with a 5.25 Å layer thickness (i.e. Eq. (38) with $z_0 = 0$ and $\Delta z = 5.25$ Å or equivalently Eq. (44) with $f_1 = 1$ $\Delta z_1 = 0$, and $\Delta z = 5.25$ Å). However, in comparison to the reference $F(E,\Omega)$ the intensity is too low at the peak and too high on the low-energy side of the peak. Assuming now that the Pt forms islands (using Eq. (38) with $f_1 = 0.365$, $\Delta z_1 = 0$, and $\Delta z = 18$ Å) one gets a much better agreement both at the peak energy and below the peak (see Fig. 14 lower left panel). From this it is then concluded that Pt forms islands with an 18 Å mean island height covering 36.5% of the surface. In the panels to the right in Fig. 14 the uncertainty in the growth parameters is explored. In one, the height is kept but the coverage is increased to 55% and in the other, the coverage is kept while the island height is decreased to 12 Å. These structures give considerably worse agreements with the reference $F(E,\Omega)$ and the actual uncertainty on height and coverage is only ~5%. From this and several other studies, it has been concluded that in general the uncertainty is typically less than ~5–10% on the determined nano-structural parameters [23].

With the availability of user-friendly software [58] that allows to quickly going through the analysis procedure, such information is easily obtained. It is non-destructive and it is very easy to follow the evolution of structures as more material is sequentially deposited onto a surface or to study the gradual change in morphology as a consequence of, e.g. chemical reactions or annealing. The latter was done in [114] where not only the growth but also the redistribu-

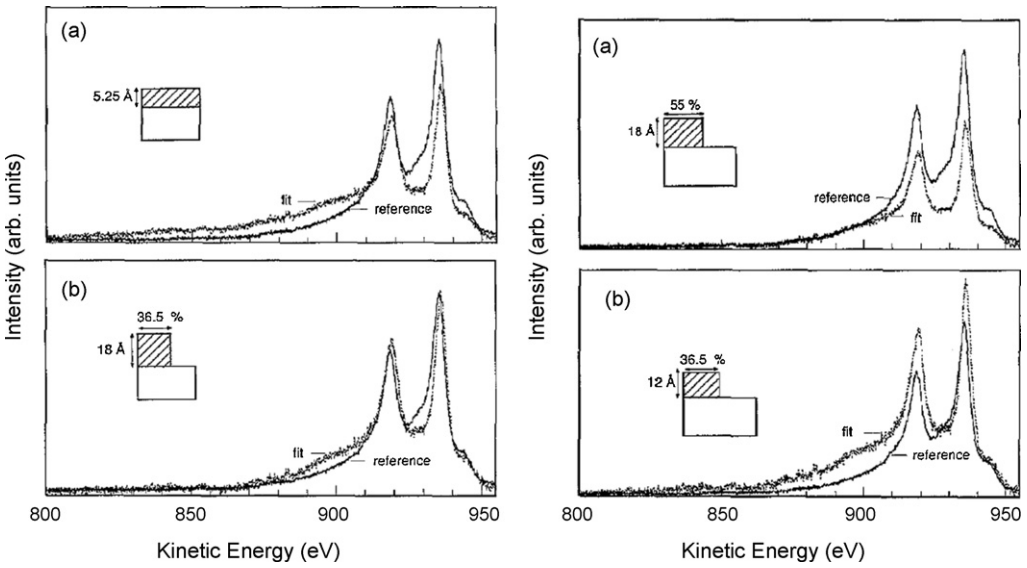

Fig. 14. Left panel: fits for Pt4d using different structures. (a) Rectangular layer on top of the substrate, 5.25 Å thick; (b) single island, 18 Å high, covering 36.5% of the surface. Right panel: fits for Pt4d using different parameters for the single island. (a) Single island 18 Å high, covering 55% of the surface; (b) single island 12 Å high, covering 36.5% of the surface (from [115]).

tion of Cu, Ag, Pt, and Au on top of and into Si were determined as a function of gradual annealing. For temperatures ~120 °C it was found that Cu and Au diffuse deep into the bulk silicon, whereas for Ag and Pt, the metal atoms remained on the surface but were found to agglomerate, i.e. the Ag and Pt islands grow higher, while the coverage decreases. It is worth to note that this information can easily be monitored in real-time as it happens.

In another example [116], the temperature-induced rearrangement of larger molecules was studied in the form of spin-coated thin films of poly(styrene)–poly(dimethylsiloxane) (PS–PDMS) diblock copolymers. The O1s spectra for one of the studied PS–PDMS polymers are shown in Fig. 15 as a function of annealing temperature. There are clear variations in the O1s peak which are due to temperature-induced rearrangements. Since only the PDMS part of the diblock copolymer contains oxygen atoms, the O1s peak intensity and shape can be used as a probe of the depth distribution of the PDMS end of the PS–PDMS molecules with respect to the surface, and in this way surface segregation of the PDMS end was studied. From the variations in the O1s peak-shape and intensity it is easy to determine the detailed PS–PDMS depth distribution [116] by analysis of spectra recorded sequentially during the annealing process and the segregation process was found to vary with the size of the polymer.

In [118], the quantity and distribution of fluorine in silicon after and during spontaneous etching with F atoms, F_2, and XeF_2 were studied. Despite its practical importance, there is still a lack of understanding of how fluorine reacts with silicon even after almost 30 years of research and development [118]. A problem is that it is difficult to detect the distribution of F in the Si lattice. Electron- or ion-based analytical techniques, e.g. Auger or secondary ion mass spectroscopy (SIMS) change the composition and distribution of fluorine so rapidly that reliable measurements are not possible. Angular-resolved photoemission could yield some information, but unlike XPS peak-shape analysis it is not valid for rough surfaces [132–135]. The XPS peak-shape analysis is however straight forward. Fig. 16 shows an example of this analysis. Note that the spectra are reversed in comparison with the other spectra shown here because they are plotted as a function of the binding energy rather than the kinetic energy. In Fig. 16 different F distributions are considered and in each case, the original spectrum, the inelastic background, and the difference are shown. The latter is the intrinsic spectrum and must consequently have near-zero intensity in a wide energy range on the low kinetic, i.e. high binding energy side of the peak. Fig. 16 shows analysis assuming that F forms a layer at the surface. The layer thickness is varied from 20 Å in (a) to 50 Å in (b) and 120 Å in (c). From this it is clear that the fluorine concentration must be significant to large depths to account for the inelastic background because the fit gets progressively better for larger thickness. However, even though there is a reasonable account for the intensity in the near-peak region for 120 Å, there is a poor account for the electron intensity in the background at larger energy loss which implies that there is a significant amount of F at depths >120 Å. This is confirmed in (d) which shows an analysis where the F concentration is taken to be exponentially varying with depth (i.e. Eqs. (32)–(34)) and in this particular example, the best fit (shown in (d)) is obtained with $f(z) = C_S[0.45 + 0.55e^{-z/10\text{Å}}]$.

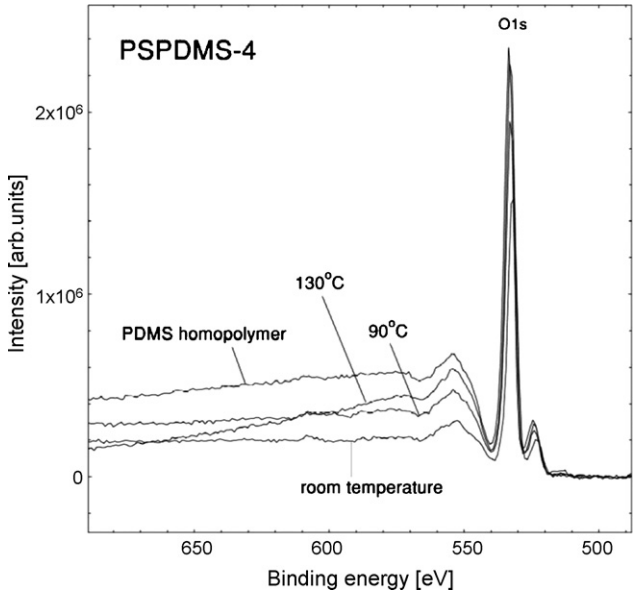

Fig. 15. O1s spectra from a PS–PDMS diblock copolymer taken at room temperature and after annealing to 90° and 130° and from a PDMS homopolymer film, from [117].

C_S and thereby also the absolute quantity of fluorine in the lattice were also estimated using photoionization cross-sections [86]. This method was also used to study the variation in the amount and depth distribution of F with type of gas, fluence and the level of n- and p-type doping of the Si [118].

Note that (in contrast to Fig. 14) the analysis in Fig. 16 is done without use of a F reference spectrum. Instead the fact was used that the intrinsic spectrum $F(E,\Omega) \sim 0$ for all energies larger than ~30 eV from the peaks.

In [119] XPS peak-shape analysis was used to study Au nano-cluster growth mechanism on polystyrene (PS) as a function of the amount of deposited Au. In addition, the authors studied the embedding of the produced nano-clusters into PS as a function of subsequent annealing at temperatures in the range from room temperature to above the PS glass transition temperature. By analysis of the Au 4f peak, the Au coverage and height could be determined with the same procedure as for Pt in Fig. 14. It is noted here that although in [119] the shape of the nano-cluster was modeled as a sphere using the generalized version of Eqs. (44)–(46) with multiple islands of varying height, the analysis is not sensitive enough to discriminate between a sphere and a cube as long as the volume is identical (this is actually also mentioned in [119] but it is worth to stress in the present context because the figures in [119] might give this impression). Thus with peak-shape analysis, only the three primary parameters that describe the main characteristics of the nano-structure are determined with high accuracy (see also the first paragraph of this section and [23]). In the present case these three parameters are the gold coverage, height and concentration. However all information can be deduced from the determined island height and coverage. Thus, taking the height as the nano-cluster diameter, the nano-cluster density can readily be calculated from the coverage. The determined Au nano-cluster size and density are shown in Fig. 17 for different amounts of Au deposition. XPS peak-shape analysis gives this information without the need for any other complementary and time-consuming techniques such as AFM, transmission electron microscopy (TEM) and the destructive cross-sectional TEM technique. For one of the samples, the authors measured the TEM image which is also shown in Fig. 17. Both the cluster size and cluster density which can be determined from this image agrees well with that determined by XPS. However the XPS analysis is much faster. It is also very easy to determine the embedding of the Au nano-particles into the PS substrate as the temperature is increased. To do this, Eq. (38) is applied and z_0 and Δz are varied until a good agreement with the reference intrinsic $F(E,\Omega)$ (determined from analysis of the XPS spectrum from a pure Au foil) is obtained. The result is seen in Fig. 18 which shows that the 25 Å nano-particles are embedded deeper than the larger 55 Å particles at a given temperature. Thus the method is efficient to study quantitatively how metal nano-clusters grow, diffuse and distribute on and in a polymer as a function of cluster size and temperature. The information is obtained without the need for any other complementary and time-consuming technique such as AFM, TEM and cross-sectional TEM. Therefore, besides being fast and non-destructive, it can stand-alone and is also suitable to monitor and control the degree of intermixing of metal-clusters and polymers which is of high technological importance [119].

The spectra in Fig. 9 above were taken from thin ZnO films deposited by plasma-enhanced chemical vapor deposition on different substrates [83,135]. The analysis was done with Eqs. (44)–(49) (using the QUASES software package [58]) and it was found (with analysis similar to that in Fig. 14) that ZnO grows in the form of islands. The determined island height and surface coverage for growth on sapphire is shown in Fig. 19. Here the island height is shown vs. surface coverage. Dashed lines in the figures correspond to fixed amount of substance (AOS) (i.e. *ch* constant, as indicated). The heights *h* and coverage *c* increase gradually as the ZnO film grows thicker. As seen, analysis of the three peaks (two from atoms in the overlayer and one from atoms in the substrate) gives reasonably consistent morphologies for the ZnO films grown. The lower island height determined by analysis of the Zn2p peak for the tallest islands is consistent with the lower probing depth of the low-energy Zn2p electrons ($\lambda = 0.74$ nm) compared with the

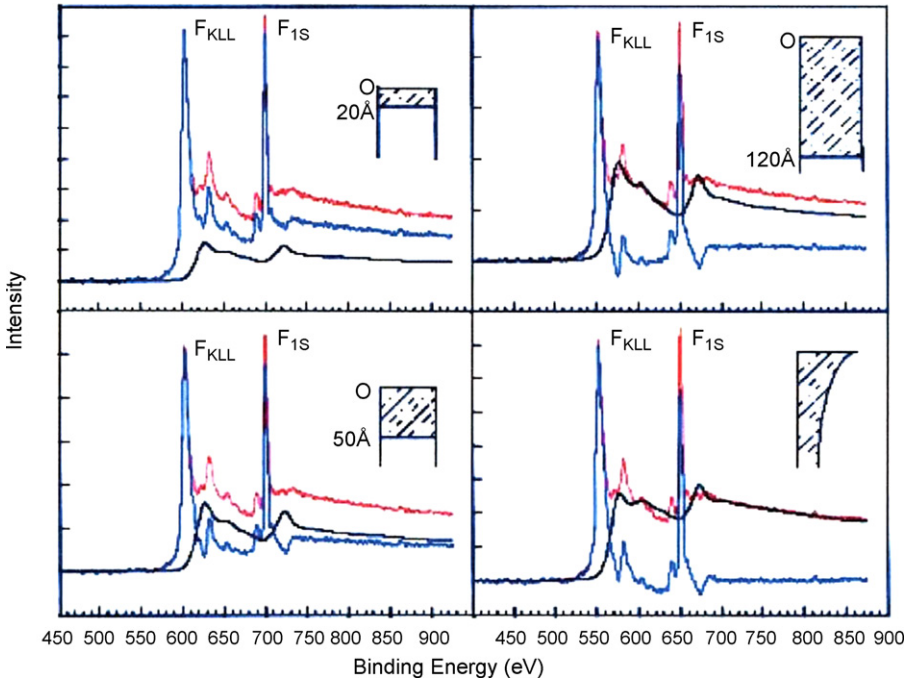

Fig. 16. XPS spectra from a 2×10^{-3} Ω cm p-type Si(1 1 1) sample exposed to XeF_2 to saturation. The same spectra with the background subtracted and the background are also shown. Analyses with different assumed F atom depth distributions are shown. Three assume a uniform distribution at the surface. The fourth assumes an exponential distribution followed by constant concentration of F in the bulk lattice. It is clear that an exponential distribution which extends deep into the bulk gives the best account for the intensity over a wide energy range, from [119].

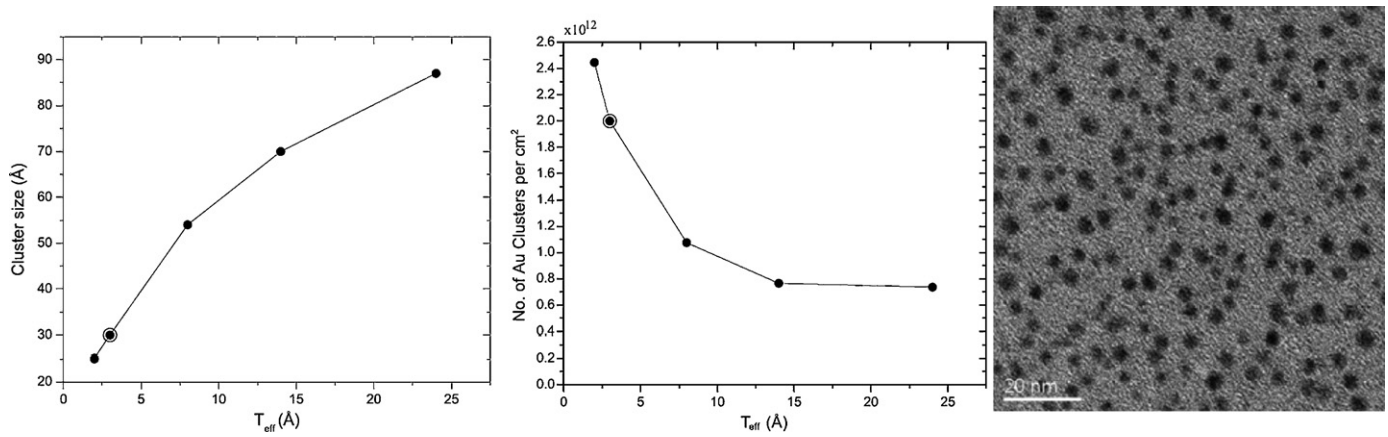

Fig. 17. Cluster size (left panel) and number of Au clusters per cm^2 (middle panel) determined from the XPS analysis for different Au depositions on PS. The TEM image in the right panel was measured for a sample with T_{eff} = 3 Å deposition and can thus be compared the centered circle values in the left and middle panels. The agreement in both cluster size and density is seen to be good, from [120].

high-energy Al KLL (λ = 2.5 nm) and Zn LMM electrons (λ = 2.0 nm). Therefore the sensitivity towards island height determination saturates for heights ≥3–4λ, i.e. ∼2.5 nm for Ni2p.

In [135] the determined amount of substance (AOS) found by XPS peak-shape analysis was compared to the AOS determined with RBS and XRF. As seen in Fig. 20 there is an almost perfect linear relation between the AOS determined with the three techniques. The absolute amounts of substance determined by RBS and XRF, however, are consistently factors of 2.1 and 1.5 lower than those determined by XPS peak-shape analysis. The deviations could be due to inaccurate calibration, uncertainty in the density of the ZnO films as well as in λ. We note here that, in general, the determined depths change linearly with the applied λ, i.e. if λ is increased by 30% the height of the structures and the AOS will also increase by 30%. The linear relations in Fig. 20 show that the relative AOS is in perfect agreement for the three techniques. For most practical applications, the discrepancy in the absolute values is however not important because local instrumental calibrations are used.

In another earlier inter-technique comparison [136], Ag and Au were deposited in varying amounts onto the (1 1 1) surface of a Ni single crystal. The amounts of deposits were determined by a quartz crystal microbalance (QCM). For both systems, the spectra were analyzed and compared to intrinsic reference spectra from pure Ag, Ni, and Au samples. In all cases, the corrected spectra were found to agree extremely well in both peak-shape and absolute intensity using the layer-by-layer plus island growth (Stranski–Krastanov) and the growth-structural parameters were determined. From the determined growth structure the total amount <*Dx*> (see Fig. 21) of Ag or Au in the film could be determined and this was found to be proportional to the observed QCM frequency shift to within ∼10%. As seen very consistent amounts were determined from analysis of all peaks from both the overlayer and the substrate.

A similar comparison [137] was made between XPS peak-shape analysis and RBS with respect to the average thickness of Au-layers in the range of 5–100 Å deposited on Ni. By peak-shape analysis of the Au4d XPS peaks, the structure and amount of Au was determined and this was compared to the Au thickness determined with RBS. The deviation between XPS and the mean value of the RBS thickness showed good quantitative agreement to within ∼7% for depths up to 7–8λ.

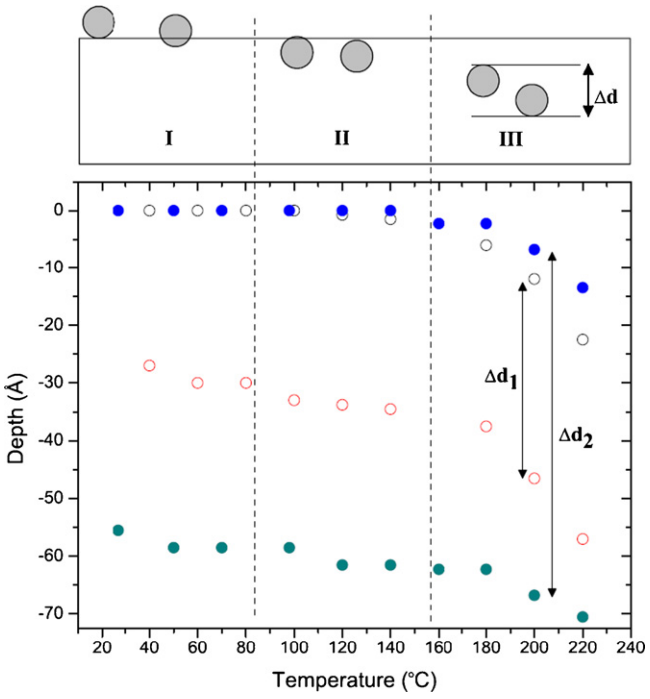

Fig. 18. Depth profile for 2 Å (open circles) and 8 Å (solid circles) (i.e. 25 and 55 Å Au nano-cluster diameter) Au deposition as a function of temperature. Δd_1 and Δd_2 are the depth interval over which the nano-clusters are distributed, from [120].

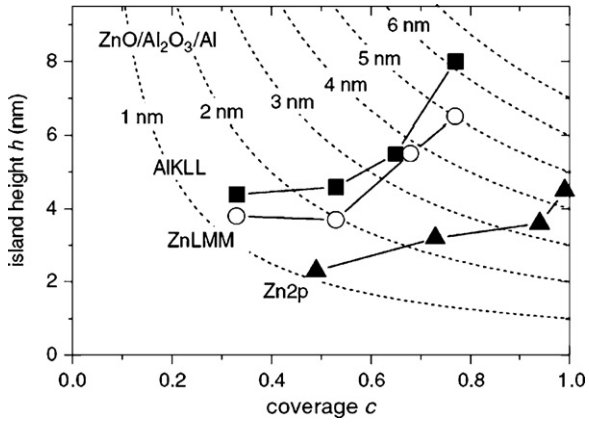

Fig. 19. Island height *h* vs. surface coverage *c* obtained from analysis of the spectra in Fig. 9 taken after sequentially growth of thicker layers of ZnO on alumina. The quantification obtained from analysis of the Zn LMM, and Al KLL peaks is indicated by circles and triangles, respectively. Dashed curves correspond to a fixed amount of material, from [83].

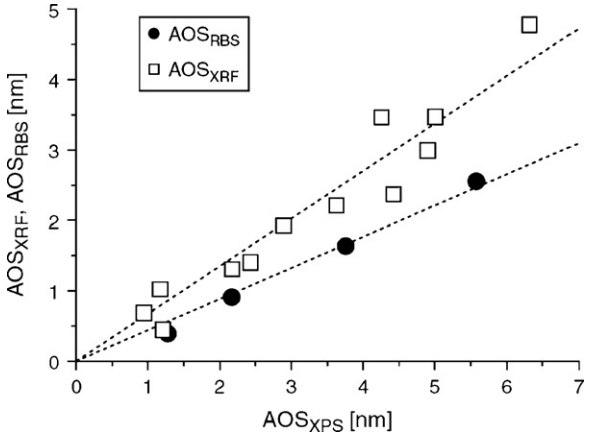

Fig. 20. Correlation between the AOS_{XPS} determined from XPS peak-shape analysis and AOS_{XRF} (open squares) and AOS_{RBS} (full circles). The straight lines are linear regressions to both sets of data passing through the origin of coordinates, from [136].

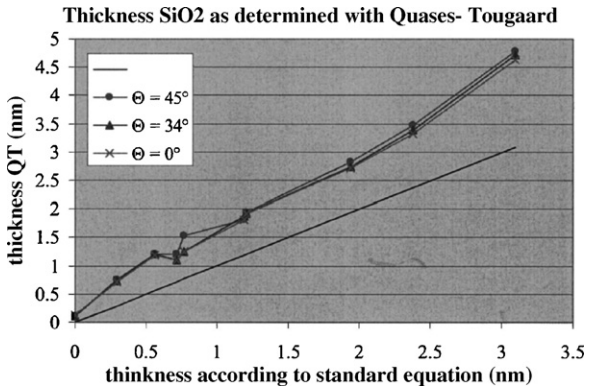

Fig. 22. Thickness "QT" of SiO_2 layers obtained by XPS peak-shape analysis of the O1s peak for 0°, 34°, and 45° emission angle, plotted against the nominal thickness, from [140].

A similar comparison of ultrathin SiO_2 layers on Si in the range from ~0.5 to ~8 nm was studied with different techniques (RBS, ellipsometry, TEM and XPS) [138,139]. Fig. 22 shows the oxide thickness ("QT") determined from XPS peak-shape analysis of the O1s peak compared to the thickness ("standard equation") determined from analysis of the ratio of the peak-area of elemental Si2p and oxidized Si2p by a formula based on the exponential attenuation law in Eq. (1) [139]. As seen in Fig. 22, peak-shape analysis of XPS spectra taken at three different angles of emission (0°, 34° and 45°) gave practically identical film thicknesses. There is a good linear agreement between thicknesses obtained with the techniques. Similar to the ZnO films (see Fig. 20), the absolute values determined with different techniques are off by a constant factor. Again, for most practical analysis purposes, only changes in the relative film thicknesses are important because a local instrument calibration will usually be applied which will eliminate the deviation as long as it is a constant factor.

The peak-shape technique was used to study changes in surface composition during oxidation [105–107,109,130]. A recent example is a quantitative *in situ* investigation of the initial oxidation stages on three FeCrNi-alloy surfaces, focusing on the effect of minor alloying elements [105]. The composition and morphology of the nano-scale surface oxides were determined quantitatively by peak-shape analysis using the QUASES software [58]. An example of the fitting procedure for one alloy composition is shown in Fig. 23. By this type of analysis quite detailed information on the nano-structures was obtained for different alloys as seen in the lower panel of Fig. 23 (see [105] for details).

Note that, rather than removing the extrinsic electrons (as in Figs. 14 and 16), the method in Section 4.1 was used in Fig. 23, i.e. the spectra are modeled by Eq. (10) and reference spectra of the various metal and oxide peaks were used as input spectra in these calculations.

6. Approximate algorithms for spectral inversion

The set of equations presented in Section 4 are exact. They may be solved efficiently by proper application of numerical fast Fourier transformation methods and in this way provide detailed quantitative information as also seen in the above examples. However, for some applications it may be of interest to use a simpler set of approximate inversion algorithms published earlier [55,56,81,140]

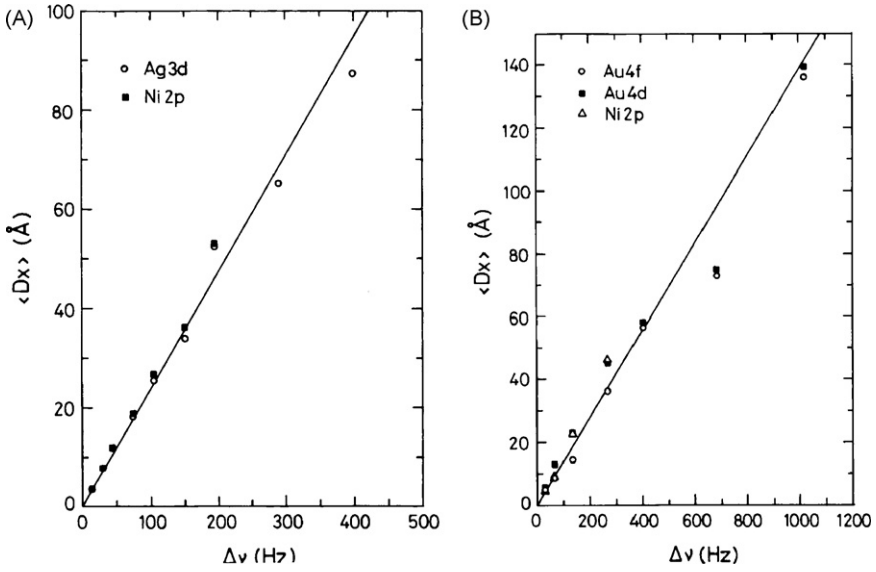

Fig. 21. (A) The total amount (*Dx*) of evaporated Ag on Ni(1 1 1) as determined by peak-shape analysis of the Ag3d and the Ni2p spectra plotted against the frequency shift of the QCM. (B) The total amount (*Dx*) of evaporated Au as determined by the peak-shape analysis of the Au 4f, Au4d, and Ni2p spectra plotted against the frequency shift of the QCM, from [137].

which were obtained by expanding the expressions in Section 4 for $F(E,\Omega)$ in terms of multiple inelastic-scattering events. The complex integral over the variable s is then avoided and the formulae can readily be evaluated with simple numerical methods. These approximate algorithms are summarized in this section. To simplify the formulas, we define the convolution integral

$$KH(E) = \int_E^{E_{max}} J(E')K(E'-E)dE' \tag{50}$$

6.1.1. Exponential and homogeneous depth distribution

Many profiles may be approximately described by an exponential atom depth distribution

$$f(z) = ce^{-z/L} \tag{51}$$

In this case, the simple and exact formula, Eq. (30), applies [81] and

$$F(E,\Omega) = \frac{L+\lambda\cos\theta}{c\lambda L\cos\theta}\left[J(E,\Omega) - \frac{\lambda L}{L+\lambda\cos\theta}KH(E)\right] \tag{52}$$

6.1.2. Delta layer profile

For

$$f(z) = N\delta(z-z_0) \tag{53}$$

one obtains [140]

$$NF(E,\Omega) \cong e^{z_0/(\lambda\cos\theta)}\left[J(E,\Omega) - \frac{z_0}{\cos\theta}KH(E) + \frac{1}{2}\left(\frac{z_0}{\cos\theta}\right)^2 \times \int_E^{E_{max}} dE'K(E'-E)KH(E')\right] \tag{54}$$

6.1.3. Substrate with an overlayer

For

$$f(z) = \begin{cases} 0 & \text{for} \quad 0 < z < \Delta z \\ c & \text{for} \quad \Delta z < z \end{cases} \tag{55}$$

one obtains [56]

$$F(E,\Omega) \cong \frac{1}{c\lambda\cos\theta}e^{\Delta z/(\lambda\cos\theta)}\left\{J(E,\Omega) - \left(\frac{\Delta z}{\cos\theta}+\lambda\right)KH(E) + \left[\frac{\lambda\Delta z}{\cos\theta} + \frac{1}{2}\left(\frac{\Delta z}{\cos\theta}\right)^2\right]\int_E^{E_{max}} dE''K(E''-E)KH(E'') - \frac{\lambda}{2}\left(\frac{\Delta z}{\cos\theta}\right)^2\int_E^{E_{max}} dE'''K(E'''-E)\int_{E'''}^{E_{max}} dE''K(E''-E''')KH(E'')\right\} \tag{56}$$

6.2. Algorithm for automatic XPS data processing

Application of the above formalism and of the rigorous formalism in Section 4 is, in principle, straightforward in particular with the availability of user-friendly software [58]. However operator interaction is necessary to decide by visual inspection when a good set of structure parameters has been obtained. It is therefore not well suited for automated data processing. Automation is very important for routine analysis and in particular it is mandatory for XPS-imaging where thousands of spectra must be analyzed. In recent years there has therefore been interest in alternative algorithms which may be less accurate but which can be used for automation.

Table 3
Rules for estimating the depth profile from L, from [59,60].

L	Depth distribution
$6\lambda < \lvert L\rvert$	Almost uniform
$-3\lambda < L < 0$	Most atoms are at depths >λ
$0 < L < 3\lambda$	Most atoms are at depths <λ
If the same peak from two samples has values L_1 and L_2, then	
if $0 < L_1 < L_2$	Atoms are surface localized in both samples and are at shallower depths in sample 1 than in sample 2
if $L_1 < L_2 < 0$	Atoms are primarily in the bulk of both samples and at deeper depths in sample 2 than in sample 1

Such an algorithm, based on analysis of electron energy loss, was first suggested in [55,56] and later improved [59] and its validity has been tested experimentally [59,60] and was recently applied to 3D XPS imaging [61–63]. The algorithm is naturally less accurate than the more detailed peak-shape analysis method but it is very robust [59] and it gives an accurate determination of the amount of substance $AOS_{3\lambda}$ (i.e. the number of atoms per unit surface area) at depths z between 0 and 3λ and it gives also a depth sectioning which estimates the depth distribution of the atoms. In this method, all depth distributions are approximated as exponential, i.e. $\exp(-z/L)$ where L is a characteristic decay length for the profile. The basic idea behind the method is that Eq. (30) is an exact solution to the analysis of the spectra for all depth profiles of exponential form, and application of this to a general (not necessarily exponential) profile therefore determines the "best" exponential profile fit to the actual depth profile. If most atoms are at shallow depths, L will turn out to be small and positive, while if most atoms are at large depths, L will be small and negative. To be specific, the method is as follows: the measured spectrum, $J(E)$, is first corrected by

$$F(E) = J(E) - B_1\int_E^{E_{max}} J(E')\frac{E'-E}{\left(C+(E'-E)^2\right)^2}dE' \tag{57a}$$

where $C = 1643\,\text{eV}^2$. For polymers, and other materials (such as Si and Al) with sharp plasmon structure, the three-parameter cross-section (see Section 3.2.1) is more accurate and then

$$F(E) = J(E) - B_1\int_E^{E_{max}} J(E')\frac{E'-E}{\left(C-(E'-E)^2\right)^2 + D(E'-E)^2}dE' \tag{57b}$$

where C and D depend on the material (see Table 1).

Rather than attempting to fit the spectrum over a wide energy range, B_1 is adjusted to give zero intensity ($F(E) = 0$) at a point 30 eV below the peak centroid E_p (see Fig. 24) (in [59] it was found that the result of the analysis varies only little if this point is chosen at 20 or 40 eV rather than at 30 eV). It is simple to get a computer to do this and thus to automate the analysis. From B_1, the decay length

$$L = \frac{B_1}{B_0 - B_1}\lambda\cos\theta \tag{58}$$

is determined. Here B_0 is the value of B_1 determined from analysis, by Eq. (57a), of the spectrum from a homogeneous sample. In practice, B_0 is $\sim 3000\,\text{eV}^2$ for most materials. The depth distribution is then estimated from the rules in Table 3 [59,60]. These rules were found from a systematic study of sets of both model and experimental spectra.

This tedious systematic study of numerous sets of theoretical model spectra calculated with Eq. (10), which is the foundation behind the rules in Table 3, is largely unpublished [141] but some of these as well as the experimental proof of their practical validity are found in [59,60]. A negative value of L corresponds to a depth

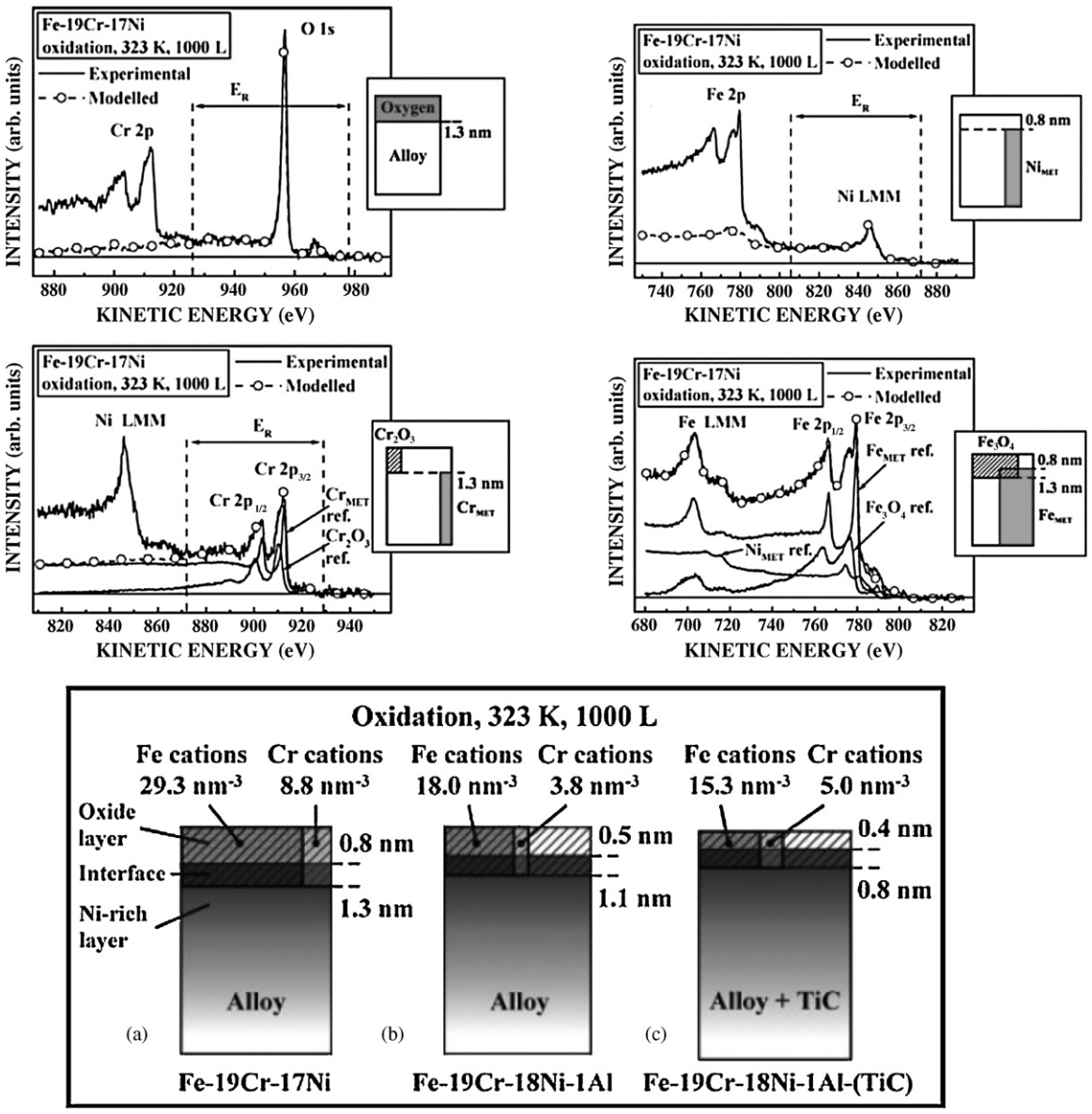

Fig. 23. Surface oxide morphology determined by inelastic electron background analysis after 1000 L O_2 exposure at 323 K for (a) Fe–19Cr–17Ni, (b) Fe–19Cr–18Ni–1Al and (c) Fe–19Cr–18Ni–1Al–(TiC). Upper panels show examples of the peak-shape analysis of individual peaks and the lower panel shows the determined structure. Interface denotes the depth range where both metal atoms and cations are present, from [105].

distribution that increases with depth within the analyzed depths (i.e. for z up to $\sim 5\lambda$). The accuracy is enhanced if, for a given system, the value B_0 is fine-tuned by replacing it by B_1^H where B_1^H is determined by analysis, from Eqs. (57a) and (57b), of a spectrum from a sample that is known to have a homogeneous atom distribution.

The *absolute* amount of substance within the outermost $\sim 3\lambda$ is [59]

$$(\mathrm{AOS})_{3\lambda} = \frac{L + \lambda\cos\theta}{1 - e^{-(3\lambda\cos\theta + L)/(L\cos\theta)}} A_p \frac{c_H}{A_p^H}(1 - e^{-3\lambda/L}) \tag{59}$$

where the peak-area is

$$A_p = \int_{E_{p-30\,\mathrm{eV}}}^{E_{\max}} F(E)dE \tag{60}$$

and A_p^H is the peak-area from a solid with a homogeneous atomic distribution of density c_H. If the objective is to find the *relative* $(\mathrm{AOS})_{3\lambda}$ in a set of samples, then it is not necessary to use a reference sample and determine c_H/A_p^H. It is often convenient to define an equivalent film thickness

$$d = \frac{\mathrm{AOS}_{3\lambda}}{c_H} \tag{61}$$

which is the thickness of the material if it were distributed as a uniform film with the same atom density as in the reference. If c_H is in atoms/nm^3 and λ is in nm, then AOS is in atoms/nm^2 and d is in nm.

The algorithm is exact to the extent that the depth distribution is exponential. However it gives a good measure for the amount of substance even if the depth profile deviates considerably from an exponential. This was shown in [59] for experimental spectra produced by placing the same $\sim$1 nm thick Au-layer at varying depths in a Ni matrix. The obtained L values agreed with the expected depth profile and the error in $(\mathrm{AOS})_{3\lambda}$ was found to be only $\sim$15% when this method is used. This should be compared to an error of up to 900% when the morphology effect is neglected and the amount of substance is taken to be proportional to the Au4d peak-area.

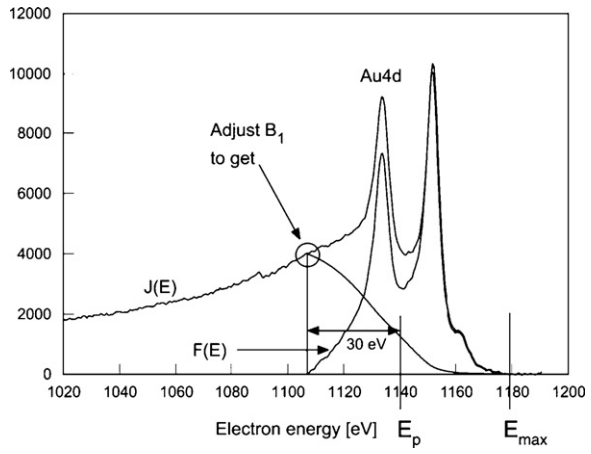

Fig. 24. Definition of the parameters used in Eq. (57), from [59].

Another experimental test was done in [60] by application to analysis of thin films of varying thickness (in the range ~0.5–10 nm) of Au evaporated on a Ni polycrystalline sample. The film thicknesses had previously been determined by both the more detailed XPS peak-shape analysis method in Section 4 and by RBS. Spectra from five samples and from pure Au and Ni reference samples taken in the Ni2p and Au4d energy regions are shown in Fig. 25 (upper left panels). The spectra were analyzed with Eq. (57a). Examples of analyzed Ni2p and Au4d spectra are shown in Fig. 25. Note also that although the Ni2p intensity for samples 5 and 4 are very low, analysis of these spectra is still straightforward and can easily be automated as seen in the right-hand panels of Fig. 25. The detailed outcome of this analysis is given in [60]. In brief, it is found that the result for both $(AOS)_{3\lambda}$ and the rules in Table 3 were in very good agreement with the known nano-structures of these samples.

7. Application to 3D XPS imaging

XPS imaging has become of increasing interest in the past decade due to both improvements in data-acquisition and subsequent processing. In particular, it is important for nanotechnological applications to determine the depth distribution on a nano-meter scale accurately. Most XPS imaging is done by plotting the peak intensity measured for each pixel. This may give erroneous results. Thus, for a nano-structured sample where different pixels have depth distributions of Au atoms as in Fig. 1 in Section 1, since the Au4d peak intensity is identical for all pixels, an XPS image based on peak intensities from such a nicely nano-structured sample would show no contrast. Improved imaging of film thickness by ARXPS [142] has been achieved. This, of course, will work fine for rather flat surfaces but for rough or nano-structured surfaces, the shadowing effect will ruin the depth information in the XPS signal at non-normal emission angles. Images where the peak-shape is taken into account using ratios of peak-area to background signal [144] for each pixel, have also been obtained [143]. Recently the algorithm in Section 6.2 was applied and this will now be discussed.

The algorithm in Section 6.2 produces two numbers for each pixel, namely the characteristic depth L and the $AOS_{3\lambda}$ and those are used together with the rules in Table 3 to produce several images of the structure as a function of depth. In [61] it was demonstrated that this produces detailed images of a plasma-patterned polymer on Teflon. The rules in Table 3 were used to qualitatively categorize the pixels into three groups: those pixels where F atoms (from Teflon) are at depths $<\lambda$ (surface), at depths $>\lambda$ (bulk), and where the F atoms have a roughly constant concentration throughout the depth interval from 0 to 3λ (homogeneous), respectively. The produced images were in good agreement with the expected qualitative nano-structure of the sample. In a further paper [62], a quantitative test of the algorithm was made by analyzing sets of Ag3d XPS spectra taken from a series of samples with different effective thicknesses of plasma-patterned octadiene (2, 4, 6 and 8 nm) on a silver substrate. The width of the octadiene strip was 125 μm. The authors produced images of the amount of silver atoms in the outermost $\sim 3\lambda$ (=9 nm) of the samples as well as images of depth sections from the L values and the rules in Table 3. The latter are shown in Fig. 26, which gives a surprisingly detailed picture on the nano-depth scale of the studied structures. The first column shows pixels with $|L| > 3\lambda$ (corresponding to a roughly homogeneous distribution of Ag). And as seen very few pixels fulfill this criterion (due to sur-

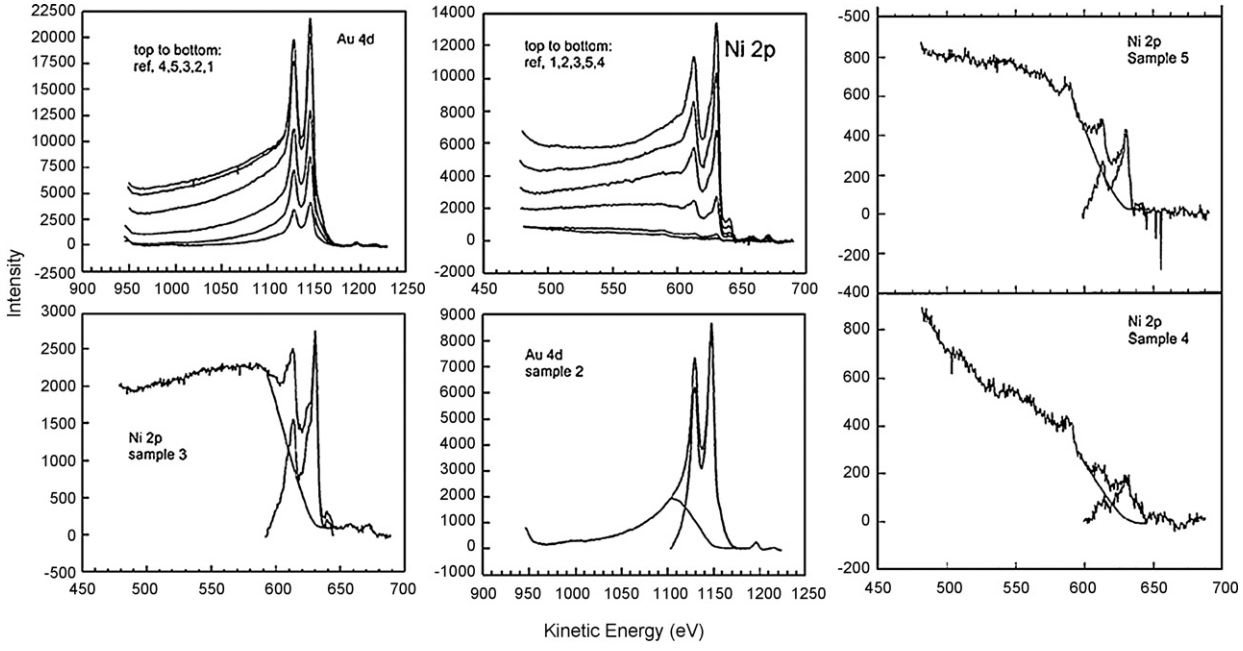

Fig. 25. Upper left panels show the Ni2p and Au4d spectra after increasing amounts of Au are deposited on five Ni substrates lower left panels show examples of analyses of the Au4d and Ni2p peaks with Eq. (57a). The right panel shows analyses of the Ni2p spectra from the two samples with the largest amount of deposited Au, from [60].

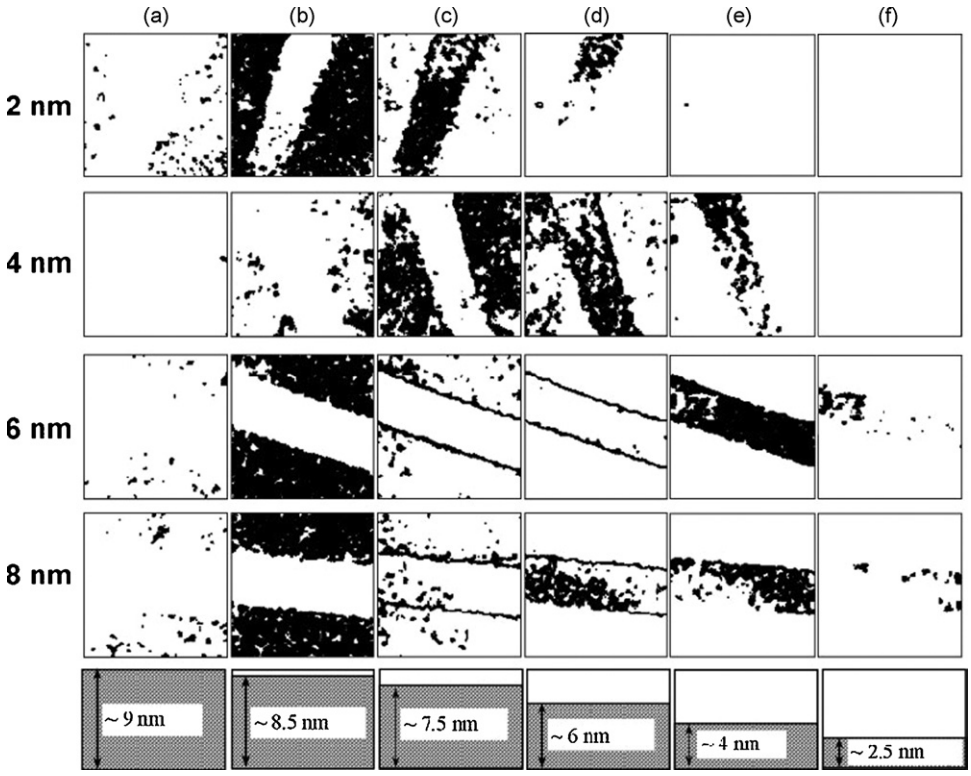

Fig. 26.. Pixels for which (a) $-1.25 < L/(3\lambda) < -1.1$, (b) $-1.1 < L/(3\lambda)^* < -0.9$, (c) $-0.9 < L/(3\lambda) < -0.78$, (d) $-0.78 < L/(3\lambda) < -0.7$, (e) $-0.7 < L/(3\lambda) < -0.62$, and (f) $-0.62 < L/(3\lambda) < -0.58$ (black means the criterion is fulfilled). The corresponding approximate depth scale is shown in the bottom, from [62].

face contamination). The following columns show pixels for which the Ag atoms are buried at increasingly larger depths. The row at the bottom shows the approximate depth scale ($3\lambda = 9$ nm) is in all cases the depth probed. Thus, e.g. column (c) of Fig. 26 shows the pixels where the overlayer is (9–7.5) nm = 1.5 nm. Consider now the top row for the sample with a nominal 2 nm thick octadiene strip, where the image in (a) shows that very few pixels have uniform Ag distribution (i.e. it is contaminated), (b) shows that the thickness of the contamination layer is ~0.5 nm and (c) together with (d) shows that the octadiene strip is ~1.5 nm in the middle and lower end and 3 nm thick at the top end, while (e) and (f) show that no pixels are covered with an overlayer >3 nm as expected. For the nominal 4 nm sample, Fig. 26 (a) shows that in no pixels is Ag uniformly distributed (i.e. all are contaminated). Fig. 26 (b), (c), and (d) shows that most pixels outside the strip are contaminated with a 1.5 nm thick layer and a few are covered with a 0.5 and 3 nm contamination layer. Fig. 26(d) and (e) show that for the 4 nm sample, the octadiene layer thickness is ~3 at one end and ~5 nm at the other; (f) shows that no pixels are covered with overlayer >5 nm. For the nominal 6 nm sample, we see from Fig. 26(a) that the distributions of Ag atoms are homogeneous in very few pixels. In Fig. 26(b) we see that the thickness of the contamination layer is ~0.5 nm. Fig. 26(c) and (d) shows that the nominal 6 nm thick octadiene strip has a border with a thickness varying from ~1.5 to 3 nm (see also Fig. 27). Fig. 26 (e) shows pixels which are covered with ~5 nm octadiene. Fig. 26f shows that for a few pixels the thickness of the octadiene overlayer is ~6.5 nm. From Fig. 26c–f, one gets an impression of the shape of the octadiene strip. For the 8 nm sample, a similar trend as for the 6 nm sample is seen. Fig. 27 shows a schematic of the structure deduced from the images of the sample with 6 nm nominal thick strip. The width across the strip in the series (b)–(c)–(d)–(e) decreases gradually which shows that the structure is tapered as in Fig. 27.

These results clearly show the potential of the method for quantitative and non-destructive imaging of the in-depth distribution of atoms with sub-nano-meter depth resolution and therefore, the ability to produce 3D images. In both Refs. [61,62], the algorithm was applied to relatively strong XPS peaks, and the data-acquisition time was also rather long. The spectra were smoothed using a quadratic,7-point Savitzky–Golay filtering [145] followed by pixel averaging. However, this procedure for noise-reduction may not be sufficient for imaging of atoms with a low photoionization cross-section. Furthermore, it would be a significant advantage for practical use if the data-acquisition time could be reduced, which, however, would lead to increased noise. More efficient methods for noise-reduction such as principal component analysis (PCA), which utilizes the full set of data, may be expected to give a

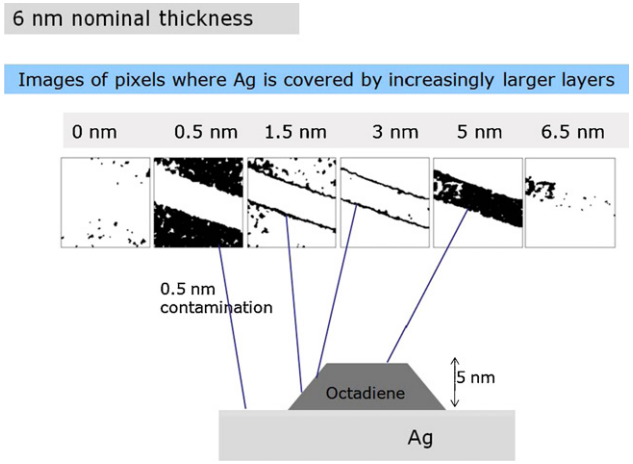

Fig. 27. Images of the pixels with different overlayer thickness for the nominal 6 nm thick octadiene and a schematic showing the interpretation of the structure. The thickness is converted from Fig. 26 by taking the probing depth 3λ(=9 nm) minus the values in the lower row in Fig. 26. Note that this shows sub-nano-meter depth resolution. The images were taken from [62].

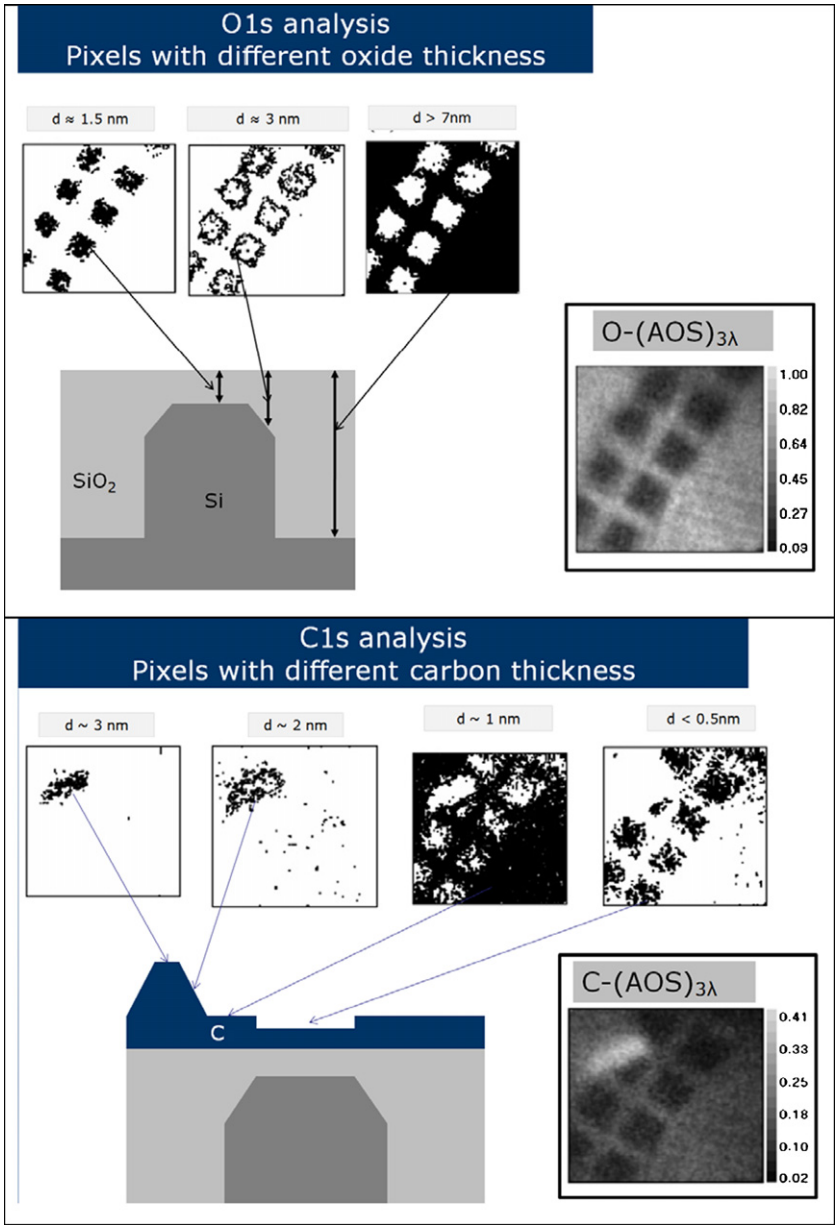

Fig. 28. 3D XPS imaging of a patterned structure made by thermally oxidizing a silicon wafer. The images of pixels with different oxide and carbon thickness were determined from analysis of the O1s and C1s peaks. The schematic shows the interpretation of the structure. The images were taken from [63].

further improvement in the signal-to-noise ratio. This was recently addressed by studying a patterned structure made on a thermally oxidized silicon wafer [63]. It was coated with positive resist and then exposed with UV light through a mask. The exposed resist was developed away and the oxide was etched with HF acid and then the remaining resist was stripped off using plasma. Spectra in 256×256 pixels from an area of $800\,\mu m \times 800\,\mu m$ of O1s, Si2p and C1s peaks which have rather low photoionization cross-sections were measured without using a high spectrometer pass energy. Therefore, the signal-to-noise level for these spectra was very low. In [63] the effect of noise-reduction procedures was studied in detail and PCA was found to be very efficient in reducing the noise in these large sets of spectra.

Images from analysis of the O1s and the C1s peaks are shown in Fig. 28. The O1s images show a thick oxide layer outside the squares and a ~1.5 nm thick oxide layer in the squares. It is interesting to see that the edges of the etched patches have a ~3 nm oxide thickness. The corresponding structure is shown schematically. Similarly the C1s images show that the C-contamination is ~1 nm thick outside and <0.5 nm thick in the etched squares. A region in the upper left corner has a ~3 nm thick C-contamination and this structure is conical as seen from the image of pixels with 2 nm thick C.

8. Conclusions

Energy-loss processes are important to interpret X-ray photoelectron spectra (XPS). First-principles quantum-mechanical descriptions have been valuable to enlighten the fundamental mechanisms behind the photoexcitation process but their complexity makes them impractical for general calculations. In recent years, a more feasible semi-classical model was used where the interaction of valence electrons with the field from both the static core-hole and the moving photoelectron is described by the dielectric function of the medium. With this model, calculations for general materials are straightforward provided the dielectric function is known.

There are in principle two origins to the energy-loss structure. The first is due to the sudden creation of the core-hole and the second to the photoelectron as it moves towards the surface. The corresponding energy-loss processes are usually called "intrinsic" and "extrinsic" excitations, respectively. In addition, the presence of the surface may cause considerable changes in the energy loss spectrum as well as in the peak intensity. Model calculations show that these processes can in principle not be treated as separate effects. The dielectric-response model gives an adequate description but is impractical for fast routine XPS analysis.

The description of XPS becomes much simpler if one assumes a complete decoupling of the effects by separating them into two or three processes, i.e. first the core-electron is excited followed by the second step in which the electron is transported to nearby the surface and finally, in the third step, it escapes through the surface region and travels in the vacuum to the electron energy analyzer. A further simplification is obtained in the two-step model, where the excitations in the third step are replaced by bulk excitations for paths up to the surface–vacuum interface and the excitations while the electron moves in the vacuum are ignored. Although the extrinsic/intrinsic contributions to the energy loss structure vary considerably with energy, geometry and depth, it turns out that the two-step model is valid to describe the *changes* in both peak intensity and energy-loss structure caused by variations in the depth distribution of excited electrons.

The change in energy spectra in the two-step model depends on the inelastic-scattering cross-section. Calculations from the dielectric function or determination from experiments are possible but in practical applications, the composition varies along the path the electron follows which complicates the description considerably. This problem is simplified with the introduction of the concept of universality classes of cross-sections.

Rigorous algorithms to calculate the XPS energy spectra within the two-step model were developed almost two decades ago. The extrinsic contributions will vary with the depth distribution of photoemitting atoms and from analysis of this, quantitative information on the depth distribution of atoms can then be determined. Since this method is non-destructive and all information is found from analysis of a single spectrum, it is possible to monitor composition changes on the nano-scale as they happen for example during deposition, annealing or chemical reactions.

Application of this formalism is straightforward and a few examples were discussed. Automatic data analysis is important for routine XPS work and mandatory for XPS-imaging where thousands of spectra must be analyzed. We then discussed a recently proposed simpler algorithm which is less accurate but which is suitable for automation, and its recent applications to quantitative 3D XPS imaging. This algorithm is also expected to be useful in the development of expert systems for automated XPS analysis.

References

[1] D. Briggs, J.T. Grant (Eds.), Surface Analysis by Auger and X-ray Photoelectron Spectroscopy, IM-Publications, 2003, ISBN 1 901019047.
[2] In: J.C. Rivière, S. Myhra (Eds.), Handbook of Surface and Interface Analysis: Methods for Problem-solving, 2nd edition, Taylor and Francis CRC Press (2009). ISBN 13:978-0-8493-7558-3.
[3] S. Tanuma, C.J. Powell, D.R. Penn, Surf. Interface Anal. 17 (1991) 911.
[4] S. Tanuma, C.J. Powell, D.R. Penn, Surf. Interface Anal. 21 (1993) 165.
[5] S. Tanuma, C.J. Powell, D.R. Penn, Surf. Interface Anal. 21 (1994) 165.
[6] C.J. Powell, A. Jablonski, NIST Electron Inelastic-Mean-Free-path Database, SRD, 71, Version 1.1, National Institute of Standards and Technology, Gaithersburg, MD, 2000.
[7] R.H. Ritchie, Phys. Rev. 106 (1957) 874.
[8] F. Yubero, S. Tougaard, Phys. Rev. B 46 (1992) 2486.
[9] A.C. Simonsen, F. Yubero, S. Tougaard, Phys. Rev. B 56 (1997) 1612.
[10] G. Gergerly, M. Menyhard, S. Gurban, A. Sulyok, J. Toth, D. Varga, S. Tougaard, Surf. Interface Anal. 33 (2002) 410–413.
[11] W.S.M. Werner, W. Smekal, H. Störi, C.E. Eisenmenger-Sittner, J. Vac. Sci. Technol. A 19 (2001) 2388.
[12] N. Pauly, S. Tougaard, F. Yubero, Surf. Interface Anal. 37 (2005) 1151.
[13] N. Pauly, S. Tougaard, Surf. Sci. 602 (2008) 1974.
[14] K. Salma, Z.J. Ding, H.M. Li, Z.M. Zhang, Surf. Sci. 600 (2006) 1526.
[15] J. Zemek, P. Jiricek, B. Lesiak, A. Jablonski, Surf. Sci. 562 (2004) 92.
[16] N. Pauly, S. Tougaard, Surf. Interface Anal. 41 (2009) 23.
[17] S. Tougaard, J. Vac. Sci. Technol. A14 (1996) 1415.
[18] S. Tougaard, P. Sigmund, Phys. Rev. B25 (1982) 4452.
[19] S. Tougaard, A. Ignatiev, Surf. Sci. 129 (1983) 355.
[20] S. Tougaard, Surf. Sci. 162 (1985) 875.
[21] S. Tougaard, Surf. Interface Anal. 11 (1988) 453.
[22] S. Tougaard, H.S. Hansen, Surf. Interface Anal. 14 (1989) 730.
[23] S. Tougaard, Surf. Interface Anal. 26 (1998) 249.
[24] P.H. Citrin, G.K. Wertheim, Y. Baer, Phys. Rev. B 16 (1977) 4256.
[25] P. Steiner, H. Höchst, S. Hüfner, Z. Phys. B 30 (1978) 129.
[26] D.R. Penn, Phys. Rev. Lett. 38 (1977) 1429.
[27] S. Tougaard, Phys. Rev. B34 (1986) 6779.
[28] W.S.M. Werner, Surf. Sci. 526 (2003) L159.
[29] C.N. Berglund, W.E. Spicer, Phys. Rev. 136 (1964) A1030.
[30] B.I. Lundqvist, Phys. Kondens. Mater. 9 (1969) 236.
[31] S. Doniach, M. Sunjic, J. Phys. C. Solid State 3 (1970) 285.
[32] J.L. Gersten, N. Tzoar, Phys. Rev. B 8 (1973) 5671.
[33] J.J. Chang, D.C. Langreth, Phys. Rev. B 8 (1973) 4638.
[34] P.J. Feibelman, Phys. Rev. B 7 (1973) 2305.
[35] G.D. Mahan, Phys. Rev. B 11 (1975) 4814.
[36] J. Pardee, G.D. Mahan, D.E. Eastman, R.A. Pollak, Phys. Rev. B 11 (1975) 3614.
[37] J.E. Inglesfield, Solid State Commun. 40 (1981) 467.
[38] L. Hedin, J. Michaels, J. Inglesfield, Phys. Rev. B 58 (1998) 15565.
[39] L. Hedin, J.D. Lee, J. Electron Spectrosc. Relat. Phenom. 124 (2002) 289.
[40] W.S.M. Werner, Surf. Interface Anal. 31 (2001) 141.
[41] T. Fujikawa, H. Arai, Chem. Phys. Lett. 368 (2003) 147.
[42] F. Yubero, S. Tougaard, Phys. Rev. B 71 (2005) 045414.
[43] F. Yubero, L. Kover, W. Drube, Th. Eickhoff, S. Tougaard, Surf. Sci. 592 (2005) 1.
[44] Z. Berényi, L. Kövér, S. Tougaard, F. Yubero, J. Tóth, I. Cserny, D. Varga, J. Electron Spectrosc. Relat. Phenom. 135 (2004) 177–182.
[45] L. Kövér, M. Novák, S. Egri, I. Cserny, Z. Berényi, J. Tóth, D. Varga, W. Drube, F. Yubero, S. Tougaard, W.S.M. Werner, Surf. Interface Anal. 38 (2006) 569.
[46] F. Yubero, J.M. Sanz, B. Ramskov, S. Tougaard, Phys. Rev. B 53 (1996) 9719.
[47] F. Yubero, D. Fujita, B. Ramskov, S. Tougaard, Phys. Rev. B 53 (1996) 9728.
[48] S. Hajati, O. Romanyuk, J. Zemek, S. Tougaard, Phys. Rev. B 77 (2008) 155403; S. Hajati, O. Romanyuk, J. Zemek, S. Tougaard, Phys. Rev. B 77 (2008) 249904.
[49] S. Tougaard, F. Yubero, QUEELS-XPS: Software to Calculate Intrinsic, Extrinsic and Surface Effects in XPS Ver. 1 (2009) http://www.quases.com.
[50] J. Lindhard, K. Dan, Vindesk. Selsk. Mat. Fys. Medd. 28 (1954) 8.
[51] S. Tougaard, I. Chorkendorff, Phys. Rev. B35 (1987) 6570.
[52] S. Tougaard, J. Kraaer, Phys. Rev. B43 (1991) 1651.
[53] S. Tougaard, Solid State Commun. 61 (1987) 547.
[54] S. Tougaard, Surf. Interface Anal. 25 (1997) 137.
[55] S. Tougaard, J. Electron Spectrosc. Relat. Phenom. 52 (1990) 243.
[56] S. Tougaard, J. Vac. Sci. Technol. A8 (1990) 2197.
[57] W.S.M. Werner, W. Smekal, C.J. Powell, NIST Database for the Simulation of Electron Spectra for Surface Analysis, SRD, 100, Version 1.0, National Institute of Standards and Technology, Gaithersburg, 2005.
[58] S. Tougaard, QUASES: Software for Quantitative XPS/AES of Surface Nanostructures by Analysis of the Peak-shape and the Background, Ver. 5.1 (1994–2008). http://www.quases.com.
[59] S. Tougaard, J. Vac. Sci. Technol. A21 (2003) 1081.
[60] S. Tougaard, J. Vac. Sci. Technol. A23 (2005) 741.
[61] S. Hajati, S. Coultas, C. Blomfield, S. Tougaard, Surf. Sci. 600 (2006) 3015.
[62] S. Hajati, S. Coultas, C. Blomfield, S. Tougaard, Surf. Interface Anal. 40 (2008) 688.
[63] S. Hajati, S. Tougaard, J. Walton, N. Fairley, Surf. Sci. 602 (2008) 3064.
[64] R.H. Ritchie, A. Howie, Philos. Mag. 36 (1977) 463.
[65] F. Yubero, S. Tougaard, E. Elizalde, J.M. Sanz, Surf. Interface Anal. 20 (1993) 719.
[66] F. Yubero, J.M. Sanz, J.F. Trigo, E. Elizalde, S. Tougaard, Surf. Interface Anal. 22 (1994) 124.
[67] S. Tougaard, F. Yubero, Surf. Interface Anal. 36 (2004) 824.
[68] H. Ritchie, A.L. Marusak, Surf. Sci. 4 (1966) 234.
[69] J.L. Gervasoni, N.R. Arista, Surf. Sci. 260 (1992) 329.
[70] C. Biswas, A.K. Shukla, S. Banik, V.K. Ahire, S.R. Barman, Phys. Rev. B 67 (2003) 165416.
[71] Handbook of Optical Constants of Solids, Edward Palik Academic Press, New York, 1985.
[72] S. Tougaard, F. Yubero, QUEELS-$\epsilon(k,\omega)$-REELS: Software to Determine the Dielectric Function from Experimental REELS, Ver. 3.0 (2003–2007), http://www.quases.com.
[73] L. Landau, J. Phys. (Moscow) 8 (1944) 201.
[74] E. Oran Brigham, The Fast Fourier Transform, Prentice-Hall, Englewood Cliffs, NJ, 1974.
[75] S. Tougaard, QUEELS-XS-REELS: Software for Determination of the Inelastic-scattering Cross-section by Analysis of REELS Ver. 2.1 (2003), http://www.quases.com.
[76] W.S.M. Werner, Surf. Sci. 588 (2005) 26.
[77] T. Nagatomi, K. Goto, Appl. Phys. Lett. 87 (2005), Art. No 224107.
[78] M.P. Seah, Surf. Sci. 420 (1999) 285.

[79] H.S. Hansen, S. Tougaard, Surf. Interface Anal. 17 (1991) 593.
[80] H. Bischel, R.P. Saxon, Phys. Rev. A11 (1975) 1286.
[81] S. Tougaard, Surf. Sci. 139 (1984) 208.
[82] S. Tougaard, Appl. Surf. Sci. 101 (1996) 1.
[83] A.I. Martin-Concepción, F. Yubero, J.P. Espinós, A.R. González-Elipe, S. Tougaard, J. Vac. Sci. Technol. A21 (2003) 1393.
[84] S. Tougaard, W. Braun, E. Holub-Krappe, H. Saalfeld, Surf. Interface Anal. 13 (1988) 225.
[85] M.P. Seah, Surf. Interface Anal. 20 (1993) 243.
[86] J.H. Scofield, J. Electron Spectrosc. 8 (1976) 129.
[87] R.F. Reilman, A. Msezane, S.T. Manson, J. Electron Spectrosc. 8 (1976) 389.
[88] M.P. Seah, I.S. Gilmore, S.J. Spencer, Surf. Interface Anal. 31 (2001) 778.
[89] I.M. Band, Y.I. Kharitonov, M.B. Trzhaskovskaya, Atom. Data Nucl. Data Tables 23 (1979) 443.
[90] A. Jablonski, S. Tougaard, Surf. Interface Anal. 26 (1998) 17.
[91] A. Jablonski, S. Tougaard, Surf. Interface Anal. 26 (1998) 374.
[92] A. Jablonski, S. Tougaard, Surf. Interface Anal. 22 (1994) 129.
[93] S. Tougaard, A. Jablonski, Surf. Interface Anal. 25 (1997) 404.
[94] A. Jablonski, S. Tougaard, J. Vac. Sci. Technol. A8 (1990) 106.
[95] C.J. Powell, A. Jablonski, SIA 33 (2002) 211.
[96] R.F. Egerton, Electron Energy-loss Spectroscopy in the Electron Microscope, 2nd edition, Plenum Press, New York, 1996, p. 174.
[97] G.T. Orosz, G. Gergely, S. Gurban, M. Menyhard, J. Toth, D. Varga, S. Tougaard, Vacuum 71 (2003) 147.
[98] C.M. Kwei, Y.H. Tu, C.J. Tung, Nucl. Instr. Method B 230 (2005) 125.
[99] Y.H. Tu, C.M. Kwei, C.J. Tung, Surf. Sci. 601 (2007) 865.
[100] N. Pauly, S. Tougaard, Surf. Sci. 601 (2007) 5611.
[101] N. Pauly, S. Tougaard, F. Yubero, Surf. Interface Anal. 38 (2006) 672.
[102] H.S. Hansen, A. Bensauola, S. Tougaard, J. Zborowski, A. Ignatiev, J. Cryst. Growth 116 (1992) 271.
[103] A.C. Simonsen, M. Schleberger, S. Tougaard, J.L. Hansen, A. Nylandsted Larsen, Thin Solid Films 338 (1999) 165.
[104] D. Eon, G. Cartry, V. Fernandez, C. Cardinaud, E. Tegou, V. Bellas, P. Argitis, E. Gogolides, J. Vac. Sci. Technol. B22 (2004) 2526.
[105] P. Jussila, K. Lahtonen, M. Lampimäki, M. Hirisimäki, M. Valden, Surf. Interface Anal. 40 (2008) 1149.
[106] B.P. Payne, A.P. Grosvenor, M.C. Biesinger, B.A. Kobe, N.S. McIntyre, Surf. Interface Anal. 39 (2007) 582–592.
[107] A.P. Grosvenor, B.A. Kobe, N.S. McIntyre, S. Tougaard, W.N. Lennard, Surf. Interface Anal. 36 (2004) 632.
[108] H.S. Hansen, S. Tougaard, H. Biebuyck, J. Electron Spectrosc. Relat. Phenom. 58 (1992) 141.
[109] M. Lampimäki, K. Lahtonen, M. Hirisimäki, M. Valden, Surf. Interface Anal. 39 (2007) 359.
[110] L. Hanley, Y. Choi, E.R. Fuoco, et al., Nucl. Instr. Method Phys. Res. B203 (2003) 1116.
[111] S. Tougaard, H.S. Hansen, M. Neumann, Surf. Sci. 244 (1991) 125.
[112] M. Schleberger, D. Fujita, C. Scharfschwerdt, S. Tougaard, Surf. Sci. 331–333 (1995) 942.
[113] D. Fujita, M. Schleberger, S. Tougaard, Surf. Sci. 331–333 (1995) 343.
[114] M. Schleberger, D. Fujita, C. Scharfschwerdt, S. Tougaard, J. Vac. Sci. Technol. B 13 (1995) 949.
[115] L. Kövér, S. Tougaard, J. Tóth, L. Daróczi, I. Szabó, G. Langer, M. Menyhárd, Surf. Interface Anal. 31 (2001) 271.
[116] T.H. Andersen, S. Tougaard, N.B. Larsen, K. Amdal, I. Johannsen, J. Electron Spectrosc. 121 (2001) 93.
[117] B.S. Semak, T. Jensen, L.B. Tækker, P. Morgen, S. Tougaard, Surf. Sci. 498 (2002) 11.
[118] H.F. Winters, D.B. Graves, D. Humbird, S. Tougaard, J. Vac. Sci. Technol. A25 (2007) 96.
[119] S. Hajati, V. Zaporojtchenko, F. Faupel, S. Tougaard, Surf. Sci. 601 (2007) 3261.
[120] E.R. Fuoco, L. Hanley, J. Appl. Phys. 92 (2002) 37.
[121] J.P. Espinós, A.I. Martin-Concepción, C. Mansilla, F. Yubero, A.R. González-Elipe, J. Vac. Sci. Technol. A24 (2006) 919.
[122] M. Zhou, C. Wu, P.D. Edirisinghe, J.L. Drummond, L. Hanley, J. Biomed. Mater. Res. 77A (2006) 1.
[123] E. Johanson, L. Nyborg, Surf. Interface Anal. 35 (2003) 375.
[124] J. Zemek, P. Jiricek, A. Jablonski, B. Lesiak, Appl. Surf. Sci. 199 (2002) 138.
[125] F. Garcia, F. Yubero, J.P. Espinós, A.R. González-Elipe, Appl. Surf. Sci. 252 (2005) 189.
[126] M. Del Re, R. Gouttebaron, J.P. Dauchot, P. Leclère, R. Lazzaroni, M. Wautelet, M. Hecq, Surf. Coat. Technol. 151–152 (2002) 86.
[127] K. Lahtonen, M. Lampimäki, P. Jussila, M. Hirisimäki, M. Valden, Rev. Sci. Instrum. 77 (2006) 083901.
[128] F. Yubero, A.R. González-Elipe, S. Tougaard, Surf. Sci. 457 (2000) 24.
[129] C. Gallardo-Vega, W. De La Cruz, S. Tougaard, et al., Appl. Surf. Sci. 255 (2008) 3000.
[130] S. Tougaard, W. Hetterich, A.H. Nielsen, H.S. Hansen, Vacuum 41 (1990) 1583.
[131] M. Aronniemi, J. Sainio, J. Lahtinen, Surf. Sci. 578 (2005) 108.
[132] P.J. Cumpson, in: D. Briggs, J.T. Grant (Eds.), Surface Analysis by Auger and X-ray Photoelectron Spectroscopy, SIM-Publications, Chichester, West Sussex, UK, 2003, p. 651, Chap. 23 (and references therein).
[133] S. Oswald, F. Oswald, Surf. Interface Anal. 40 (2008) 700.
[134] P. Kappen, K. Reihs, C. Seidel, M. Voertz, H. Fuchs, Surf. Sci. 465 (2000) 40.
[135] A.I. Martin-Concepción, F. Yubero, J.P. Espinos, J. Garcia, S. Tougaard, Surf. Interface Anal. 35 (2003) 984.
[136] H.S. Hansen, C. Jansson, S. Tougaard, J. Vac. Sci. Technol. A10 (1992) 2938.
[137] A. Cohen Simonsen, J.P. Pøhler, C. Jeynes, S. Tougaard, Surf. Interface Anal. 27 (1999) 52.
[138] B.S. Semak, C. van der Marel, S. Tougaard, Surf. Interface Anal. 33 (2002) 238.
[139] C. van der Marel, M.A. Verheijen, Y. Tamminga, R.H.W. Pijnenburg, N. Tombros, F. Cubaynes, J. Vac. Sci. Technol. A22 (2004) 1572.
[140] S. Tougaard, J. Vac. Sci. Technol. A5 (1987) 1230.
[141] S. Tougaard, Private communication.
[142] K. Artyushkova, J.E. Fulghum, J. Electron Spectrosc. Relat. Phenom. 149 (2005) 51.
[143] J. Walton, N. Fairley, J. Electron Spectrosc. Relat. Phenom. 148 (2005) 29.
[144] S. Tougaard, J. Vac. Sci. Technol. A 5 (1987) 1275.
[145] A. Savitzky, M.J.E. Golay, Anal. Chem. 36 (1964) 1627.